ANALYSIS OF FRICTION STIR WELDING BEHAVIOR OF ALUMINUM CERIUM ALLOY AND VIABILITY FOR INDUSTRIAL APPLICATION

By

Devany A. Sweitzer

Thesis

Submitted to the Faculty of the

Graduate School of Vanderbilt University

in partial fulfillment of the requirements

for the degree of

MASTER OF SCIENCE

in

Mechanical Engineering

May 10, 2019

Nashville, Tennessee

Approved:

Alvin M. Strauss, Ph.D.

George E. Cook, Ph.D.

DEDICATION

This thesis is dedicated to my mother for her continuous support in all that I do, to my friend Darren for always listening and providing sage advice, and to the rest of my family for always believing in me and raising me to trust I can achieve anything I put my mind to.

ACKNOWLEDGMENTS

I could not have completed this thesis without help. I am thankful to Dr. Strauss and Dr. Cook for their mentorship and guidance, and vast engineering knowledge which helped this project come to fruition. I would like to thank Adam Jarrell for providing welding and instrumentation knowledge and for being my machining/SEM/safety buddy. Gratitude is additionally owed to Kelsay Neely, whose extensive background in material science came in handy more than once, and to Connor Strawn for providing me with the occasional Trolli sour brite gummi egg candy for motivation. All the graduate students in the Vanderbilt University welding and automation lab have proven to be valuable colleagues, and invaluable companions. Finally, this project would not have been possible without the financial support provided by Vanderbilt University and the NASA Space Grant Consortium.

TABLE OF CONTENTS

LIST OF TABLES

LIST OF FIGURES

1 Introduction

1.1 Overview of Friction Stir Welding (FSW)

Friction stir welding (FSW) is a solid-state joining process that was first developed by The Welding Institute in 1991 and has expanded rapidly since, particularly in the field of aluminum. [1] Consequently, the process has found successful application in aluminum-heavy industries such as automotive, maritime, and aerospace. [2] With the FSW method, two plates of the material to be welded are clamped together, most commonly in a butt or overlap configuration (see **Figure 1**). A stirring tool with a probe and shoulder plunges into the workpiece and traverses along the length of the joint line, generating enough heat to plasticize the material while staying below the melting point. As the tool moves, the plasticized material is extruded around the tool probe and forged together under the pressure of the tool shoulder as it completes the pass. Common control parameters for FSW include tool rotation rate, traverse rate, plunge depth, axial force, and torque, but machine configuration and programming have an effect on which are used principally in the welding profile. Due to the fact that it is a solid-state process, FSW does not experience problems from resolidification like traditional welding techniques. [1] [2]

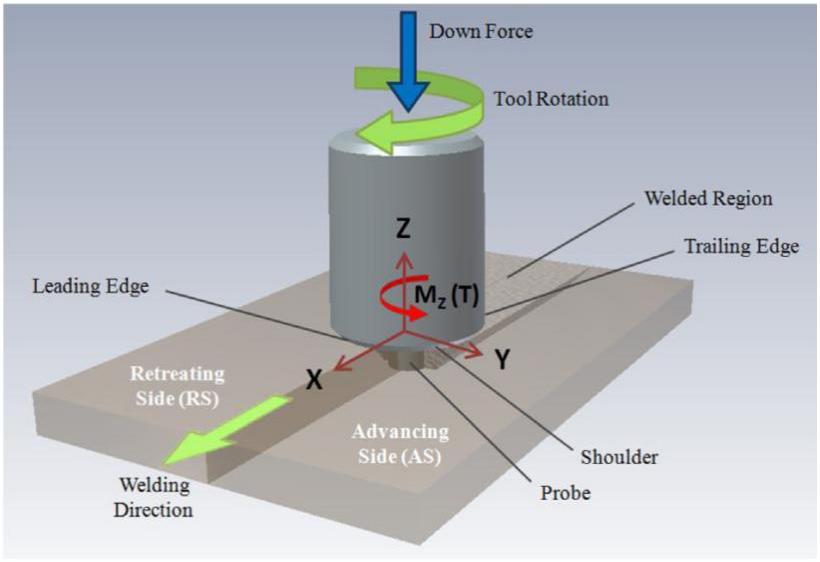

Figure 1. FSW process diagram, butt weld configuration [2]

The use of welding for joining aerospace structures was long inhibited by the difficulty of making successful welds from highly alloyed 2XXX and 7XXX series aluminum alloys, which

were classified as “non-weldable” due to poor solidification, porosity, and insufficient strength and resistance through the fusion zone. With the implementation of FSW, these limitations have been overcome for many aluminum alloys and aerospace industries have commercially produced defect-free friction stir weld joints. [1][2]

Automotive corporations have also widely begun to adopt FSW as a joining and manufacturing process. The integration of lightweight aluminum alloys into automotive assemblies allows the creation of more energy efficient systems; Ford, Mazda, BMW, and various other automobile manufacturers have taken to employing FSW for joining body structures and panels as well as manufacturing parts of varying thickness. The overall result is improved dimensional accuracy, 30% increase in weld strength (as compared to fusion welding), and a reduction in parts, weight, and post-processing. Today, implementation of FSW technologies continues to grow as researchers work to understand the behavior, modelling, and process parameter selection as it applies to an infinite variety of material joining systems. [1][2]

1.2 Current Limitations of Aluminum Alloys

Due to its light weight, low cost, and desirable mechanical properties, aluminum is very prominent in the aerospace industry. While many barriers in FSW have been overcome, the majority of commercial aluminum alloys still have problematic performance limitations. Most castable aluminum alloys are strengthened through precipitation of intermetallics formed from alloying elements added during casting. Typically, precipitate formation is closely controlled as the compounds formed critically affect the microstructure and mechanical behavior of the final material. Some of the most predominantly utilized alloying elements for aluminum are Si, Mg, and Cu. [3][4]

While these additions can strengthen the material at room temperature, several atomic percent of the intermetallics formed dissolve into the matrix at temperatures greater than 300ºC. This renders the microstructural features impermanent, causing a drop in high-temperature stability and consequently material properties. These intermetallics are also often vulnerable to coarsening, and repeated or continuous exposure to high temperatures also leads to a loss of mechanical properties. Often these limitations result in alloys that cannot be relied upon in high temperature environments. As a result, engineers designing parts for high temperature

environments like engine blocks and drive train systems often have to sacrifice efficiency by selecting heavy cast iron components, or significantly increasing cost with expensive titanium alloys. [4][5][6]

If an aluminum alloy composition was able to be formed with high mechanical property retention at temperatures exceeding 300°C, it would fill the role of a light and affordable material for high temperature applications. Prevalent high-temperature performance aluminum alloy advancements to date have been focused on the progression of alloying systems such as Al-Sc, Al-Zr, and Al-V. These alloys are more expensive to manufacture, but form strengthening precipitates which increase thermodynamic stability; however, the lattice coherence which this stability depends on still limits these alloys to operating temperatures not exceeding 300°C. [3][4][5]

In the last decade, development and production of a novel aluminum alloy with favorable high mechanical property retention at high temperatures has drastically increased. By alloying aluminum with cerium, researchers at Oak Ridge National Laboratories (ORNL) and Eck Industries have found that the resulting product is an alloy with significantly improved mechanical property retention at temperatures >300°C. These aluminum cerium (Al-Ce) alloys show exceptional castability and mechanical properties in addition to being thermodynamically stable. Cast parts of Al-Ce alloys form in thermodynamic equilibrium and stay in equilibrium until near melting; this can be attributed to the cerium-heavy intermetallic compounds precipitated during formation. [7] Unlike the precipitates formed in traditional alloying systems (Al-Si, Al-Mg, Al-Cu, etc), the precipitates formed with cerium have extremely low solubility in the aluminum matrix even as the temperature is increased: near the eutectic temperature (642°C), Cu has solubility exceeding 5% while the upper limit of solubility is 0.005% for Ce. This value is also an order of magnitude below the solubility of the top competing alloying element, Sc. [3] The large size of Ce atoms furthermore causes a diffusion coefficient approximately 10,000 times smaller than those of traditional alloying elements. The cerium precipitate's significant resistance to dissolution and diffusion prevents failure through coarsening mechanisms, while the thermodynamic stability preserves the microstructure in high-temperature environments (>500°C). [4] The outstanding high-temperature behavior of this alloy gives it strong potential to fulfill many applications currently dominated by titanium and cast iron, and the low cost of Ce would make it a valuable yet inexpensive alternative. [3][7][8]

One particular variation of aluminum cerium alloy, Al-10Si-7Ce-4.3Cu-0.4Mg, was provided by Eck Industries in the form of cast plates to be used for the friction stir welding research conducted in this thesis. Copper is a common addition for engine components where high strength and toughness are required. [8] Magnesium and silicon are commonly used together in aluminum due to high castability and precipitation of strengthening Mg_2Si phases. Research has further shown that cerium reacts favorably with Mg and Si to form thermally stable intermetallics without microstructural coarsening. [3] When all of these additions are combined in an aluminum alloy with cerium mixed in, the elements combine to form numerous intermetallic compounds with the cerium (as well as forming some of the common compounds found when cerium is not present). [8][9] The resulting alloy has many of the same strengths as the commercial alloys sans cerium, and the addition of cerium inherently increases the mechanical property retention at high temperatures. It is anticipated that due to the heavy adoption of FSW in the aerospace and automotive realms, utilization of aluminum cerium alloys in these industries will inevitably lead to the implementation of FSW on aluminum cerium alloy components and castings. Currently, there is no published research on the FSW of aluminum cerium alloys. Creating a set of optimum friction stir welding parameters for any particular material requires a significant amount of data collection and analyzation – thus there is an inherent necessity for the FSW behavior of these alloys to be properly researched, analyzed, and optimized for future implementation in manufacturing. There is currently very little knowledge regarding how cerium-heavy intermetallic compounds may affect the friction stir welding behavior of aluminum alloys. The composition, strength, and friction stir welding viability of the provided aluminum cerium alloy will be analyzed in the following chapters of this thesis.

2 Background

2.1 Literature Survey

2.1.1 History and Advantages of Al-Ce Alloys

The first studies conducted on cerium-alloyed aluminum occurred in the early 1980s; initial research showed that adding 4 wt. % cerium increased the high-temperature mechanical properties, showing improved results over competing commercial aluminum alloys (hot pressed aluminum cerium displayed a tensile strength of 300 MPa at 230ºC compared to 70-180 MPa for copper, magnesium and zinc alloyed systems). Despite the high strength at elevated temperatures, work was discontinued on this alloy due to the high cost and low availability of cerium at the time. More recently, interest in this alloy has picked up once again; the successful development of aluminum cerium alloys is speculated to not only provide a light weight material with high mechanical property retention at high temperatures, but to also stimulate positive economic effects for the cost of all rare earth elements. As the most abundant rare earth element, the more mining that is done, the cheaper cerium will get while simultaneously unearthing and lowering the cost of other rare earth elements. [4][10][11][12]

Eck Industries has obtained the license for the production of aluminum cerium alloys, and has published several works in collaboration with Oak Ridge National Laboratory addressing the behavior of these alloys with varying concentrations of cerium and other alloying additions. It has been concluded that compositional variation of aluminum cerium alloys by adding other alloying elements is possible and thus the mechanical properties and microstructure are somewhat tailorable; cerium alloys with magnesium and silicon have already shown exceptional castability and high strength. [4] As was previously mentioned, the alloy provided for this research has inclusions of silicon, cerium, copper and magnesium. Adding Mg to the binary Al-Ce alloy significantly increases the ultimate tensile strength (UTS) and yield strength (YS). Eck Industries found that with the addition of only 0.4% Mg, the UTS retention at 300ºC was increased from 50% to 80% in the binary Al-Ce alloy. Additions of Si have been found to produce the tetragonal intermetallic $Ce(Si_{1-x}Al_x)$ which has high temperature stability, and Cu is commonly used in alloys to add toughness and strength. Furthermore, a T6 heat-treated Al-12Ce-4Si-0.4Mg alloy reached a UTS of 252.3 MPa and a YS of 128.2 MPa, a substantial improvement over the binary alloy which failed at a UTS of 161.3 MPa and a YS of 57.2 MPa; this directly demonstrates the

versatility of aluminum cerium alloy systems and their ability to be manipulated for various applications.

In summary, Al-Ce alloys have exceptional castability, low cost, low weight, and superior mechanical property retention at temperatures exceeding 300^{o}C, making them an ideal replacement for a variety of engine components. [4][5][8]

2.2 VUWAL Welding Machine Operation

Figure 2. VUWAL Friction Stir Welding Machine

The friction stir welder utilized for this research is seen above in **Figure 2**. It is the main research resource of the Vanderbilt University Welding Automation Laboratory (VUWAL), and is programmed and controlled with C# and Simulink code created by current and past graduate researchers. It was originally a Milwaukee milling machine, and was extensively modified to be used for FSW. The additions of sensors, motors, and instrumentation onto the machine to achieve this are largely covered in past dissertations and theses from the lab [13][14].

Two computers are utilized with the machine. The first computer holds the C# program which provides the GUI for setting up the machine and entering weld parameters prior to welding (see **Figure 3**). The sensor data, parameters, and machine commands are then routed to the second real-time computer which is in charge of actually controlling the weld and acquiring data via a Simulink model. This Simulink Real-Time kernel provides faster data sampling and makes it possible to weld with real time constraints. On the welding (first) computer, there are multiple

weld control profiles which can be generated depending on the type of weld that is being done (butt weld, lap joint, t-joint, etc.) and what type of control is being utilized. Plunge depth, plunge rate, RPM, tilt angle, positioning, and traverse rate are set by the user prior to all welds with current programming. Due to difficulties with the general butt weld control profile on the aluminum cerium alloy welds, over the course of this research a torque control program was programmed, tested, and implemented to achieve more consistent results. This will be further discussed in Chapter 3.

During a weld, process measurements and forces are constantly output and compared to user-defined safety limits to ensure no damage comes to the tool, dynamometer, or machine from surpassing stress limits. In case of an emergency or failure, there is a redundant system for emergency machine shut off. The Kistler Rotating Cutting Force Dynamometer continuously reads and outputs the X, Y, and Z forces on the tool during a weld, while string potentiometers and a vertical calibration sensor provide position references.

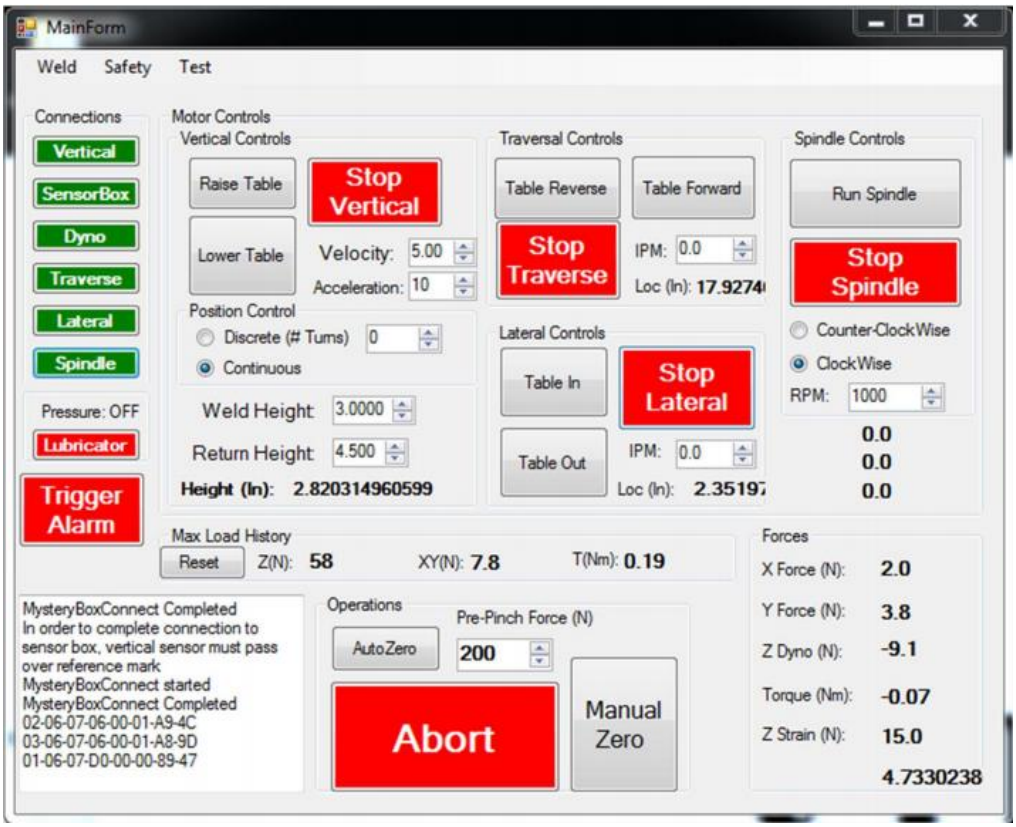

Figure 3. MainForm for welding computer GUI

2.3 Tool Geometry

There are many options when it comes to tool selection for FSW joining, as there are many design factors which can affect the consolidation and final quality of the welded material. Typical FSW tools have a contact surface consisting of a shoulder and a pin, although the geometry of these two components varies depending on application. Typically, the shoulder is around three times the diameter of the pin. A weld is started by plunging the tool until the shoulder is in contact with the workpiece. The shoulder generates localized heat in the material through the friction created by the tool's rotation, which begins to preheat the material further down the joint line. The downward axial force from the shoulder additionally works as a forging pressure for the mixed material, confining it inside the joint line and providing consolidation as the pass is completed. [1][2][15]

Before the shoulder comes in contact with the piece, the pin must plunge into the material. As the pin is plunged, it deforms and shears the material along the joint line. The large strain and heat generation from plastic dissipation around the pin plasticizes the materials; threading can then provide transport of the material around the tool. On the retreating side, material is extruded to back of the weld where it is deposited in the void left by the pin as the tool traverses. The material on the advancing side gets caught in a rotating zone and flows into the joint behind the pin as the tool traverses. The most common pin design is a threaded cylindrical pin, as it is easier to machine than other designs which may provide better weld quality, less tool wear, or faster weld speeds (round-bottom, truncated-cone, triangular, etc.). In the interest of optimizing tool design, TWI has additionally come up with unique pin designs, named Whorl, Triflute, and Trivex, which have all shown improvements on reducing displacement volume, traverse loads, and normal forces. These designs are fairly complex, making them difficult to machine. [1][16][17]

For the welding research executed in this thesis, the tool utilized has a 1-inch diameter scrolled convex shoulder with a ¼-inch diameter threaded cylindrical pin (see **Figure 4**). When using a convex shoulder, the need for a lead angle can be surpassed as the outer edge of the shoulder does not need to come into direct contact with the workpiece. Unlike tools with concave shoulders, the convex design is able to compensate for varying plunge depths, providing the possibility for controlling and varying shoulder engagement during the weld and overall providing more consistent weld quality. The inclusion of shoulder scrolls is also critical, as they help to push the material approaching the outer edge of the shoulder back in towards the center and the pin.

This prevents displaced material from escaping as flash and instead allows it to stay towards the center of the joint and be later deposited in the void. [18]

The chosen tool design incorporating a convex shoulder and cylindrical threaded pin is a logical choice. The convex scrolled shoulder design allows the possibility for high quality weld results with varying welding parameters. Since there is no current information on the FSW behavior of the aluminum cerium alloy being analyzed, the ability to manipulate parameters with bead on plate welding will be critical in forming an initial weld profile. The threaded cylindrical pin, in addition to being a reliable and proven design, is also relatively easy to machine with the available facilities at Vanderbilt.

Figure 4. FSW tool with convex scrolled shoulder and threaded cylindrical pin

2.4 Experimental Setup

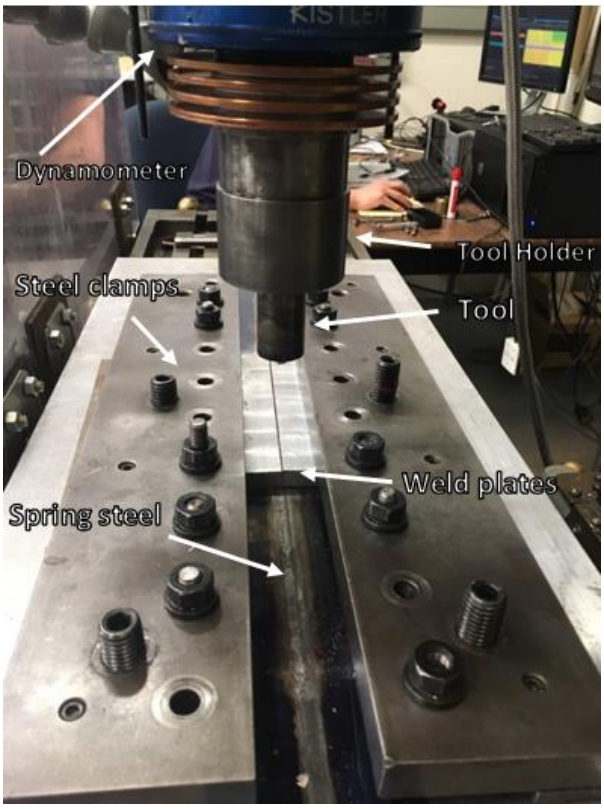

Figure 5. Photo of two pieces of aluminum cerium alloy placed and clamped for a friction stir butt weld

Figure 5 above shows the experimental layout utilized for friction stir welding in this thesis. Once the welding table is attached to the mill table (bottom), two large steel clamps are attached to the top of the welding table with bolts, with the material to be welded secured between. Spring steel is additionally slid beneath the weld plates to provide upward pressure, preventing the plates from being pushed down or apart during welding. This setup results in plates that are highly locked in position, providing security for the weld. In the configuration above, the width of the plates did not allow room for bolts immediately to the sides of the welds; additional bolts were used along the length and tightly secured to compensate.

To the left of the machine are the welding computers which are used to control and input welding parameters for the spindle, table, sensors, etc. These were previously described in section 2.2. A lubricator is run during welding to keep the spindle greased, and air is directed across the dynamometer to keep it from overheating.

3 Results

3.1 Material Properties

Eck Industries was able to provide some material property data for this aluminum cerium alloy, but due to the small sample size tested (four tensile bars) additional material testing was performed wherever possible to create a more comprehensive material property profile. Since only two relatively small cast alloy plates were provided (one 10-inch by 6-inch and one 6-inch by 6-inch both in T4 condition), they were first measured to allocate material for the maximum number of welds which could be made. The remaining material was cut off and processed for hardness and tensile bar testing.

3.1.1 Hardness Testing

Prior to any material testing or welding, some material property data was provided by David Weiss of Eck Industries on the Al-10Si-7Ce-4.3Cu-0.4Mg alloy aged to T4 condition. They reported a T4 heat treat hardness value of 85 BNH (approximately 52 HRB). Utilizing a Wilson C523R hardness tester available in the Vanderbilt structures lab, 200 additional hardness data points were taken on the pieces dedicated for material property testing. Below, **Table 1** displays the cumulative hardness testing results.

Table 1. Wilson C523R Rockwell B Hardness Test Results

Average	Min. Value	Max. Value	Standard Deviation	% Difference (Eck Industries vs. Lab Data)
54.6025 HRB	42.8 HRB	70.2 HRB	± 4.1289 HRB	5.0048 %

The final average HRB of ~54.6 is reasonably close to the value of ~52 HRB reported by Eck Industries. While the standard deviation is not egregious, the values overall were somewhat erratic, with some values in the low 40s and even low 70s; the minimum and maximum values measured were 42.8 HRB and 70.2 HRB, respectively. This variability in the data is expected to stem from the intermetallics within the material; the aluminum matrix itself is much softer than the various precipitates formed from alloying elements, particularly the cerium-heavy ones.

Consequently, it is suspected that the maximum and minimum values are so far apart due to some measurements hitting large intermetallic compounds more so than others.

3.1.2 Tensile Testing

In addition to their initial hardness data, Eck Industries sent tensile bar data for four ASTM-E8 standardized dog bones (1/4-inch thickness). [19] With the small amount of the alloy available that was not utilized for welding, three more tensile bars following the same ASTM standard were machined for additional testing at Vanderbilt. A CNC was used to cut the profile shape one inch deep into the edge of the 1/2-inch thick plate, and pieces were then cut off and surfaced with a bandsaw and milling machine to create the final specimens with 1/4-inch thickness. An extensometer was utilized to obtain the most accurate strain results for the Vanderbilt tensile data. Below, **Table 2** displays all tensile bar data accumulated to date for the Al-10Si-7Ce-4.3Cu-0.4Mg T4 alloy material profile. Shaded cells indicate data provided by Eck Industries.

Table 2. Cumulative Material Property Data for Al-10Si-7Ce-4.3Cu-0.4Mg Alloy

Specimen ID*	Max. Tensile Force (kN)	Max. Tensile Stress (MPa)	Total Elongation (%)	Modulus (GPa)
E-A1	2.70	84.806	0.500	46.738
E-A2	2.99	94.458	0.550	48.115
E-B1	2.77	87.563	0.600	60.265
E-B2	2.91	91.700	0.050	63.712
V-A	4.00	95.520	0.173	62.897
V-B	3.40	82.824	0.169	50.705
V-C	3.70	89.176	0.146	64.023
Average:	3.21	89.44	0.31	56.64
Maximum:	4.00	95.52	0.60	64.02
Minimum:	2.70	82.82	0.05	46.74
Std. Dev:	0.46	4.41	0.21	7.20

**(E – Eck Industry Data; V – Vanderbilt University Data)*

While the standard deviations show that the overall results are reasonably consistent, it can be seen that there is a noticeable variation in the results provided by Eck Industries as compared to the data collected at Vanderbilt. In communication with Eck Industries via David Weiss, it was speculated that slight adjustments in Eck Industries' testing set-up may have had an outsized impact on final tensile data due to the brittleness of the material. A reported value of ~52 HRB

would typically show triple these tensile properties in aluminum. The failure mechanism of cerium alloys has previously been reported as a two-stage yielding failure in which the Al matrix and intermetallics both initially elastically yield under low stress until a point is reached in which the intermetallics carry more of the load and eventually yield once the dislocations reach a critical density [3]. This essentially described the failure that was seen in these tensile tests, as little to no ductility was observed in the samples and the fracture surface showed brittle peaks (see **Figure 6**).

In an attempt to avoid similar issues and to get the most accurate tensile bar data at Vanderbilt, a one-inch extensometer was utilized to get precise values for elongation and strain. In **Table 2**, it can be seen that the elongation values obtained at Vanderbilt appear to be more precise than those reported by Eck Industries. It is additionally unclear if there is an error in the maximum tensile forces reported by Eck Industries due to experimental setup, but it is suspected that this may be the case since the values reported at Vanderbilt are up to a kilonewton higher. Maximum tensile stress and Young's Modulus are consistent across the board, so it is assumed that these data points at least can be considered reliable.

A stress-strain curve showing the data points for the three Vanderbilt tensile bars can be seen below in **Figure 7**.

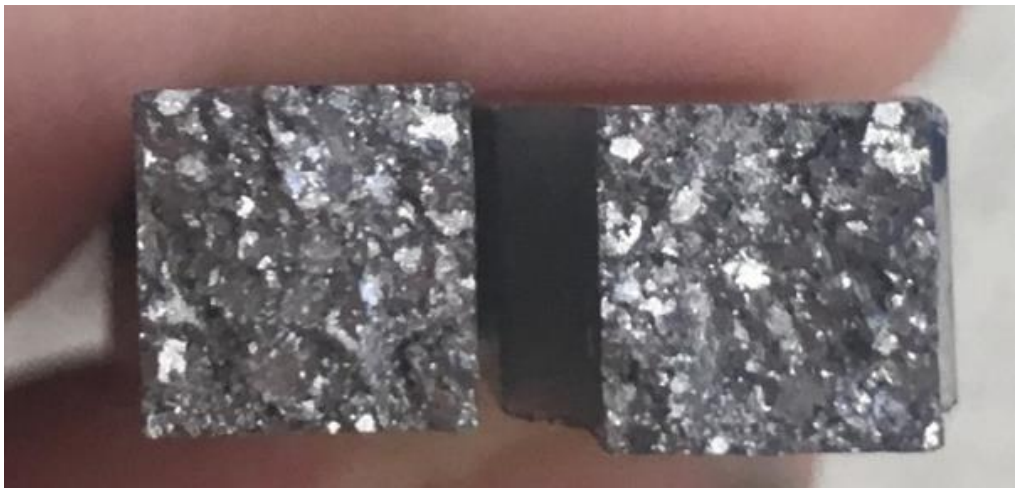

Figure 6. Fracture surface of tensile bar sample A

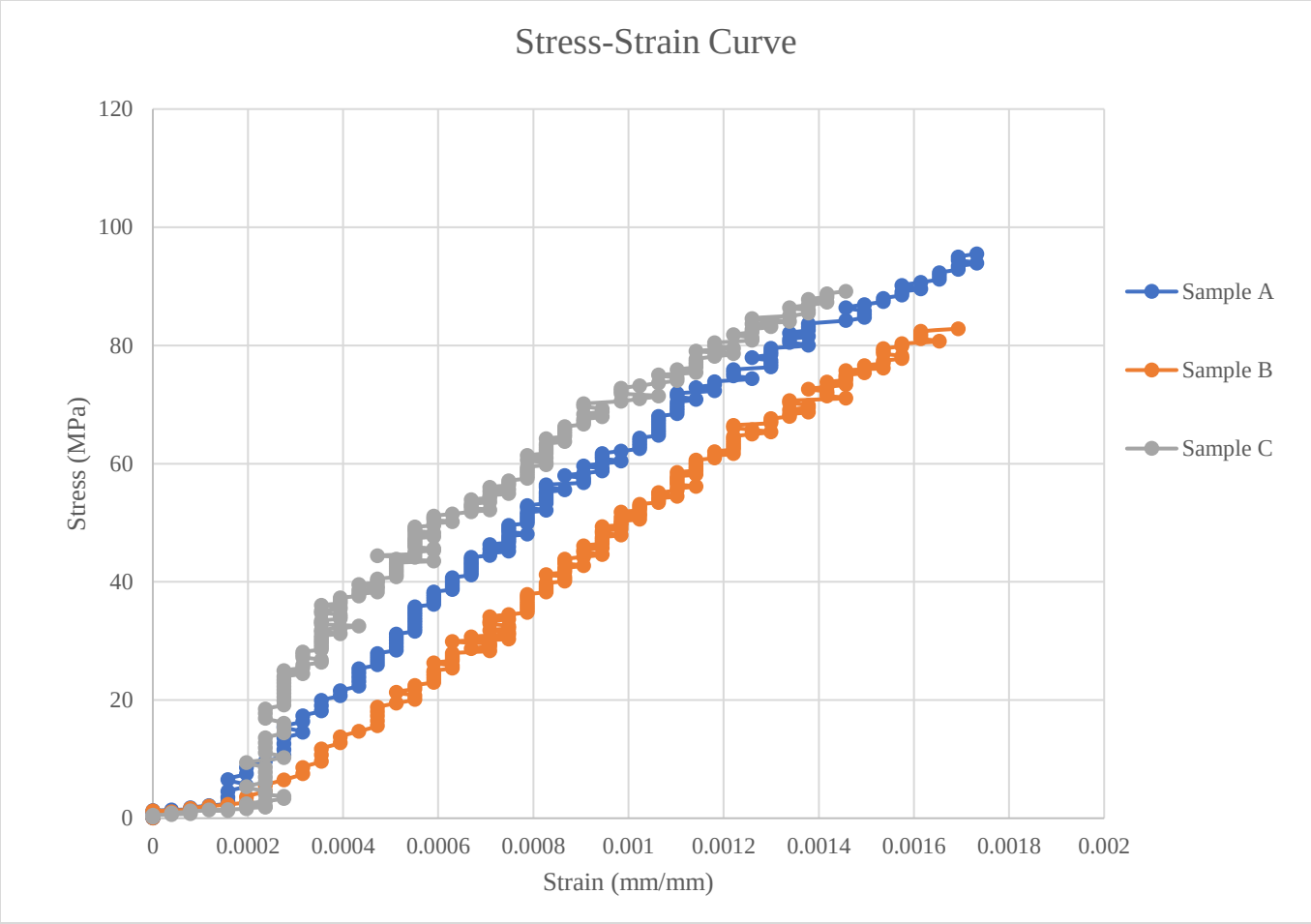

Figure 7. Stress-Strain Curve for Vanderbilt Tensile Bar Tests

3.2 Microscopy Analysis

Three small (roughly 1 cm x 1 cm) pieces of the T4 treated material were cut away from the original alloy parts and prepared for analysis with a scanning electron microscope (SEM). The pieces were cut small enough to fit on the available SEM mounting studs (1/2" in diameter) and progressively wet sanded down to a 1-micron refinement surface finish. They were then cleaned and analyzed with various detectors on the SEM to analyze surface topography, phase contrast, and elemental spectra.

3.2.1 Secondary Electron Detector (HE-SE2) Results

Utilizing a Zeiss Merlin scanning electron microscope, images were taken with the secondary electron detector (HE-SE2) to obtain a better understanding of the surface topology, as well as where inconsistencies and intermetallic variations may lie in the sample. Below, Figures **8-17** display the HE-SE2 images taken of the T4 heat treated samples. The same areas were then imaged with the backscattered electron detector (BSD) to get a comparative image displaying the phase contrast (see section 3.2.2).

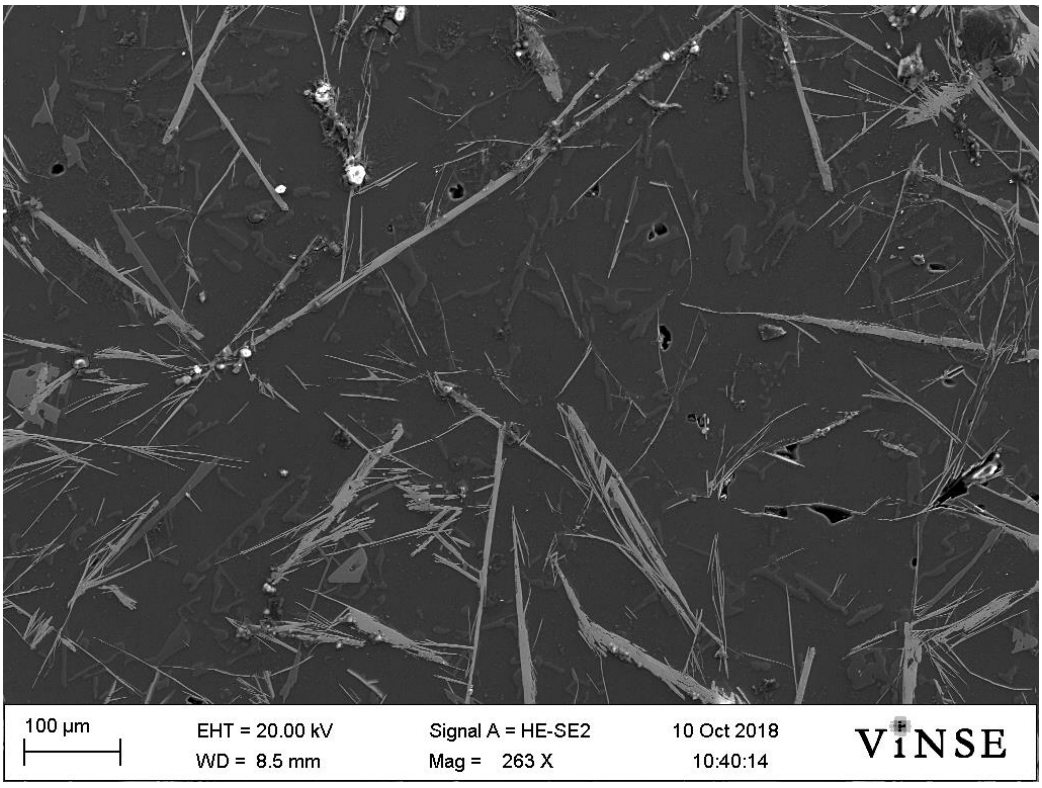

Figure 8. HE-SE2 Image 1, T4 Heat Treat (Area 1)

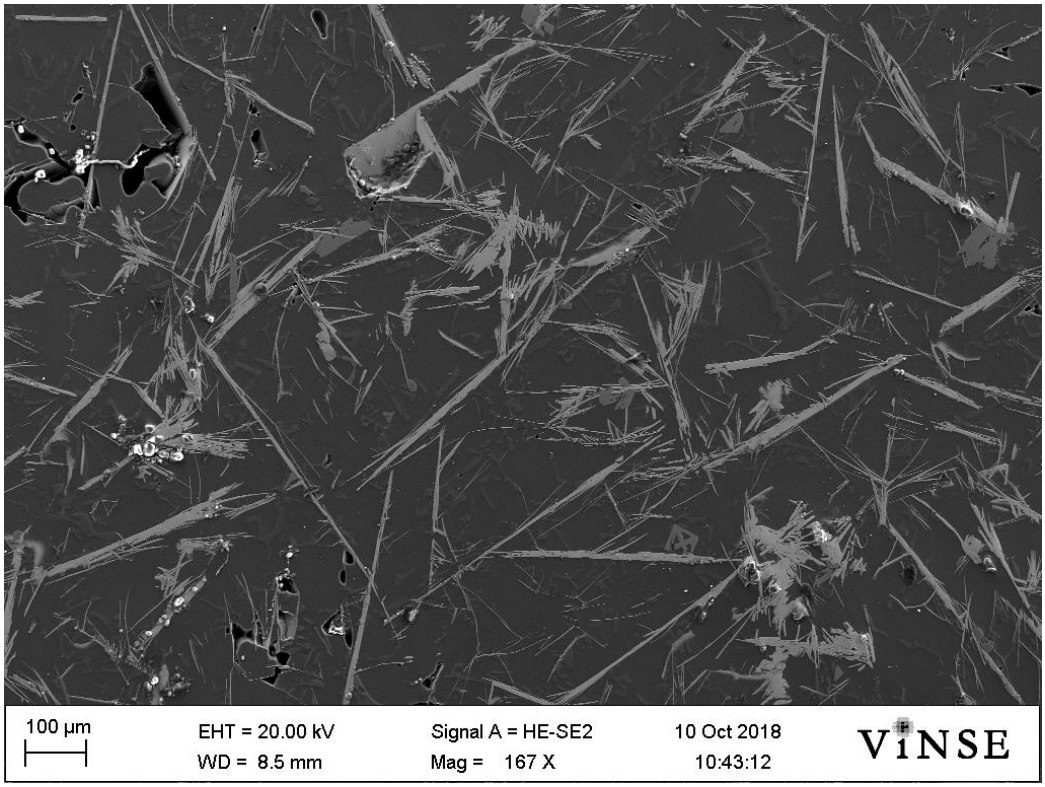

Figure 9. HE-SE2 Image 2, T4 Heat Treat (Area 2)

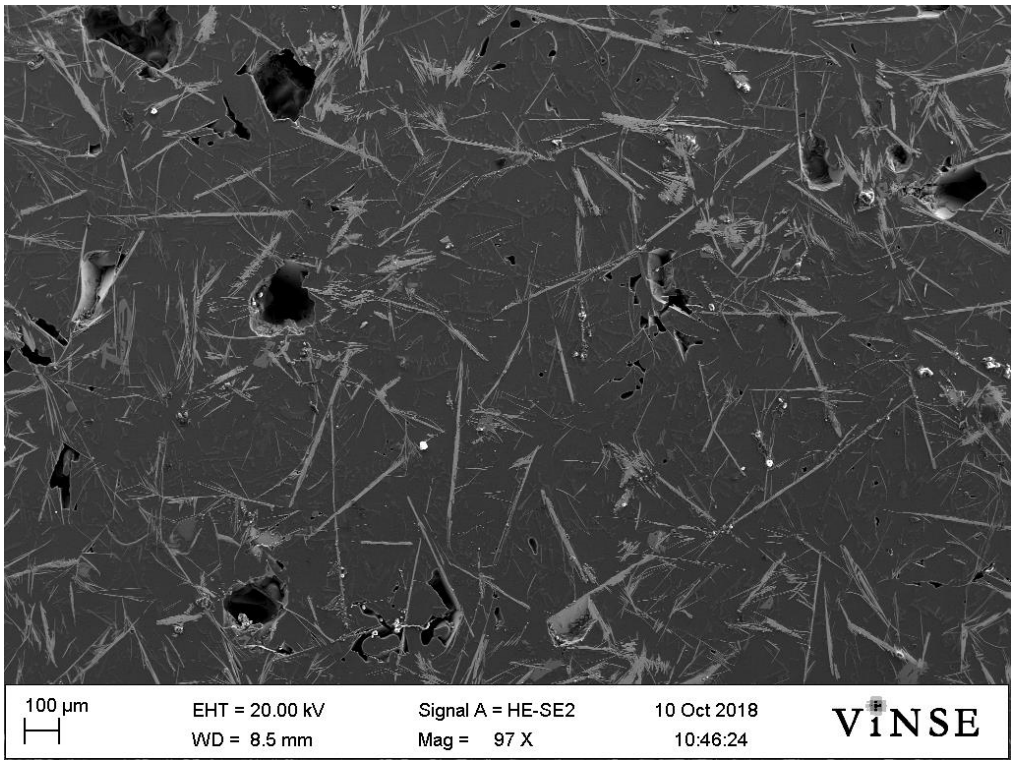

Figure 10. HE-SE2 Image 3, T4 Heat Treat (Area 3)

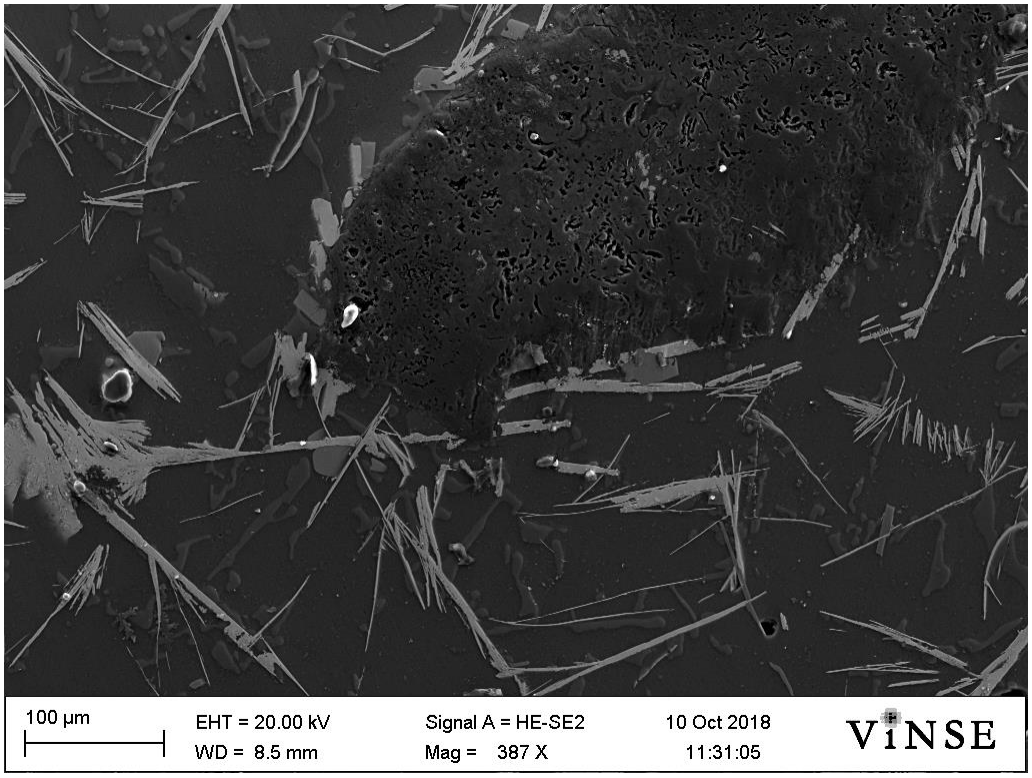

Figure 11. HE-SE2 Image 4, T4 Heat Treat (Area 4)

Figure 12. HE-SE2 Image 5, T4 Heat Treat (Area 5)

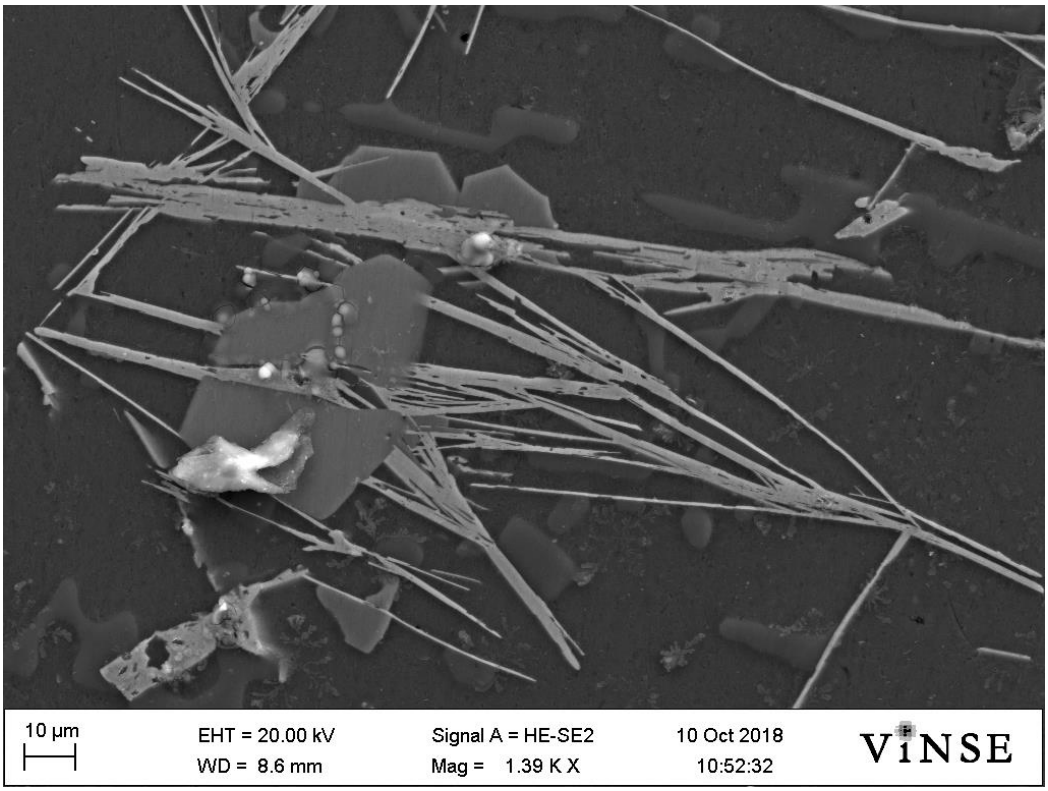

Figure 13. HE-SE2 Image 6, T4 Heat Treat (Area 6)

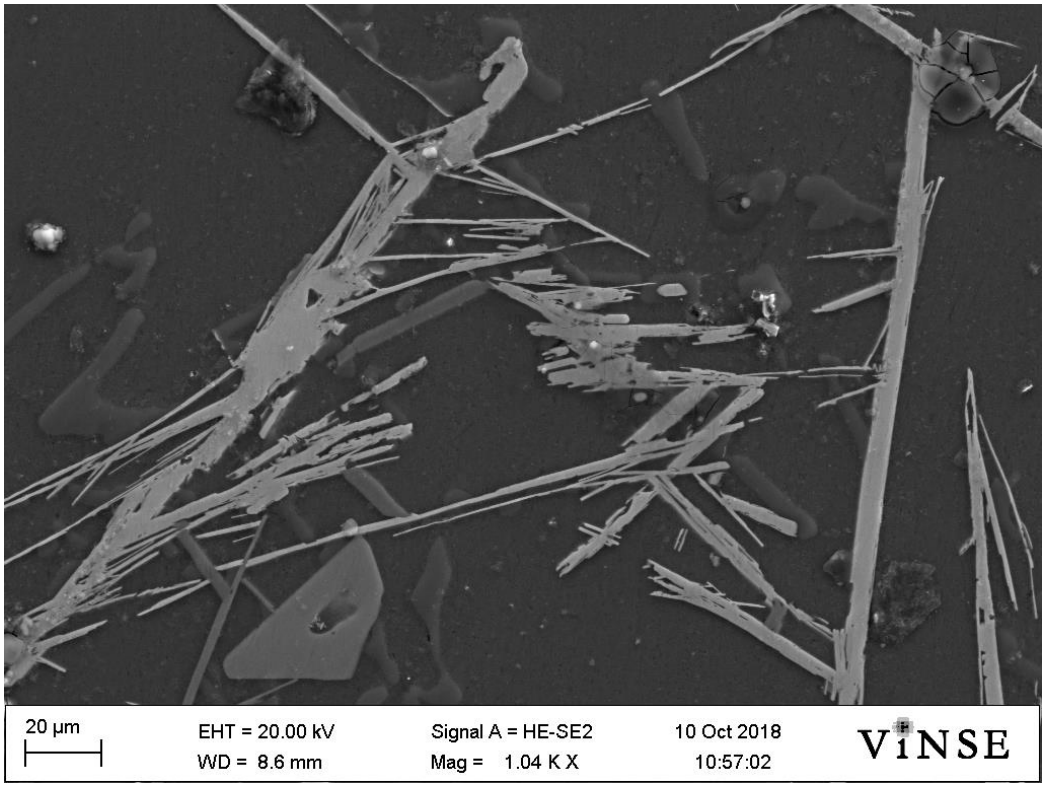

Figure 14. HE-SE2 Image 7, T4 Heat Treat (Area 7)

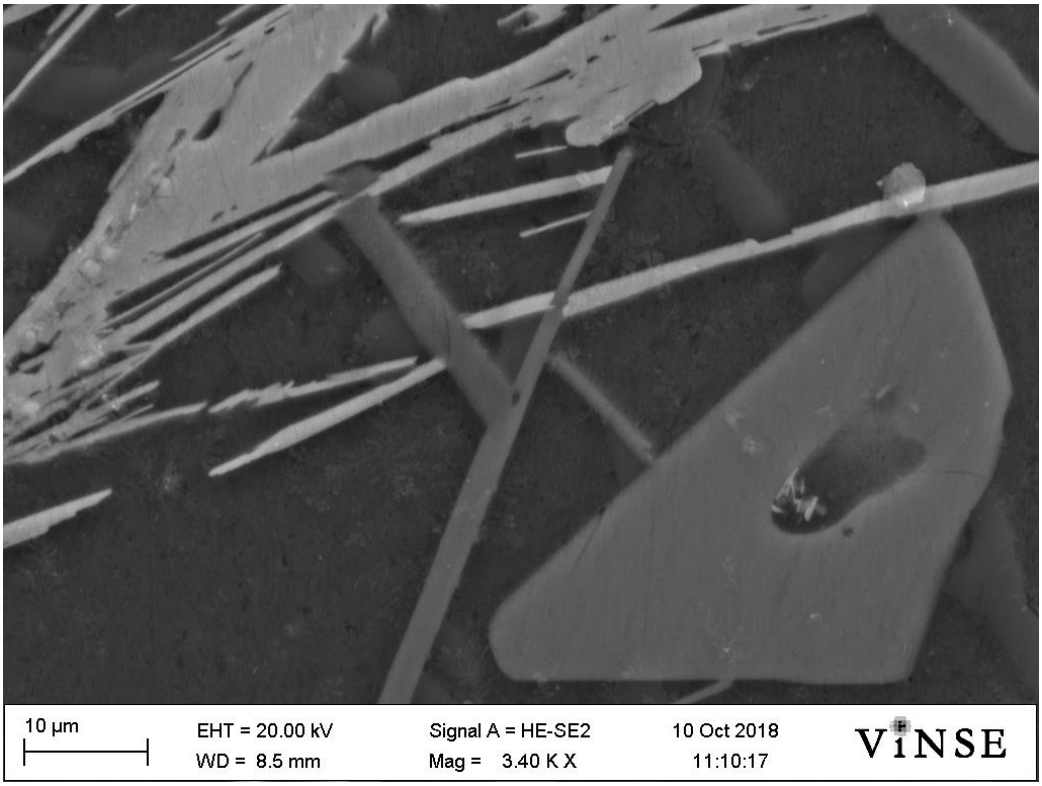

Figure 15. HE-SE2 Image 8, T4 Heat Treat (Area 8)

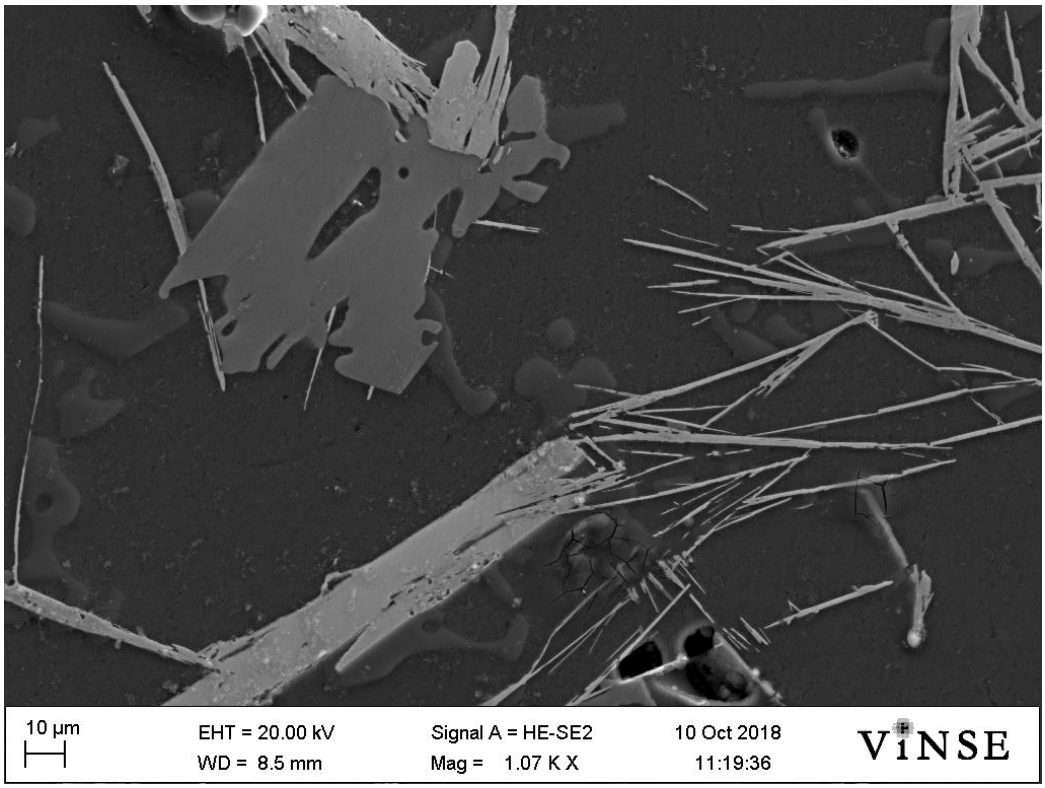

Figure 16. HE-SE2 Image 9, T4 Heat Treat (Area 9)

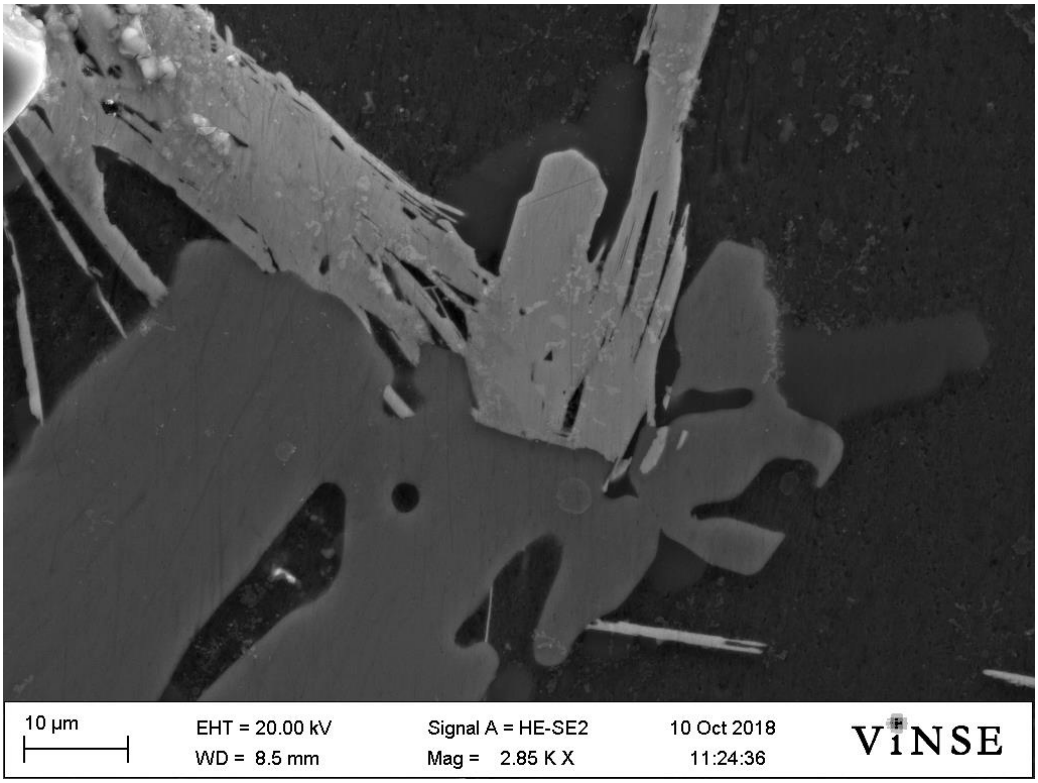

Figure 17. HE-SE2 Image 10, T4 Heat Treat (Area 10)

3.2.2 Backscattered Electron Detector (BSD) Results

Using the same Zeiss Merlin SEM, images were then taken of the same surface areas with the backscattered electron detector (BSD). Images created with this detector are formed by picking up the electrons which are elastically scattered by the atoms in the material. Atoms with a larger atomic number produce a larger amount of collisions which makes them appear brighter, resulting in an image which shows phase contrast between the various elements and intermetallics in the material. Below, Figures **18-27** display the BSD images taken and correlate them to the appropriate HE-SE2 image. From these images it can be seen that the intermetallic compounds showing up the brightest are the linear, scratch like geometries showing up consistently across the surface. These are presumed to have the highest cerium content, but elemental analysis will be further evaluated in the EDS results.

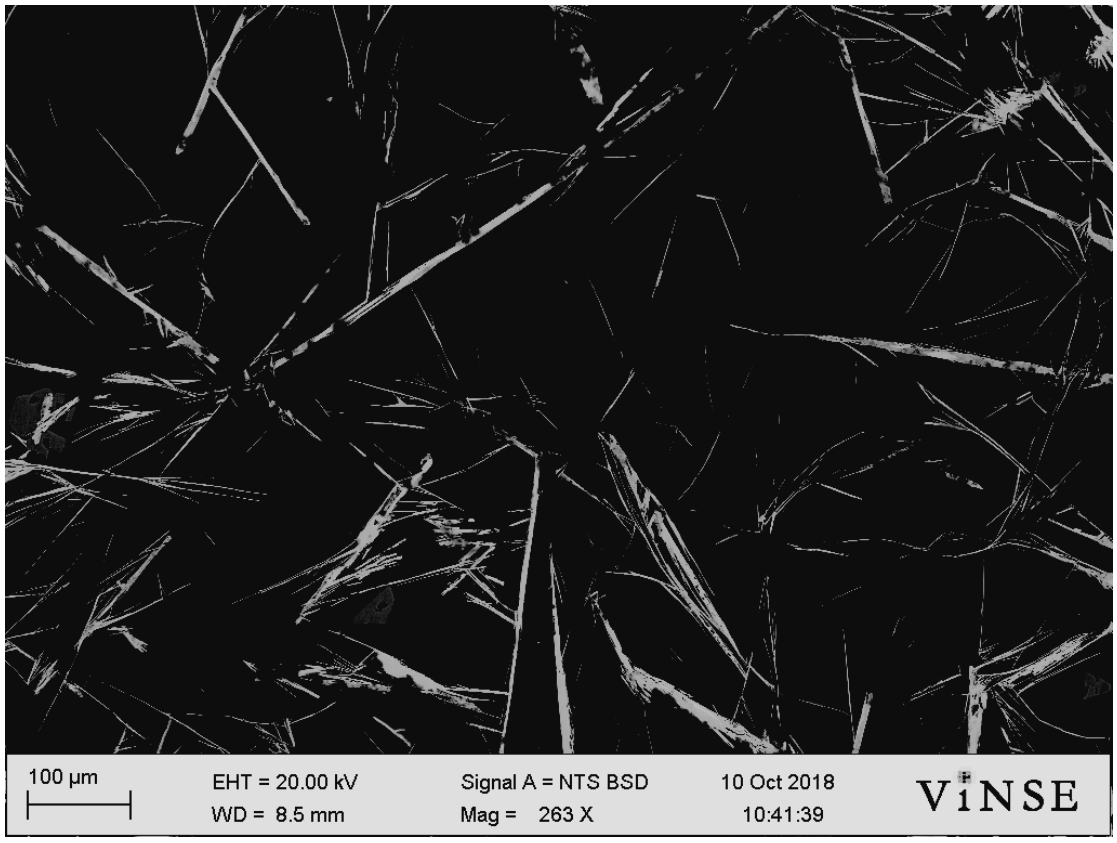

Figure 18. BSD Image 1, T4 Heat Treat (Area 1)

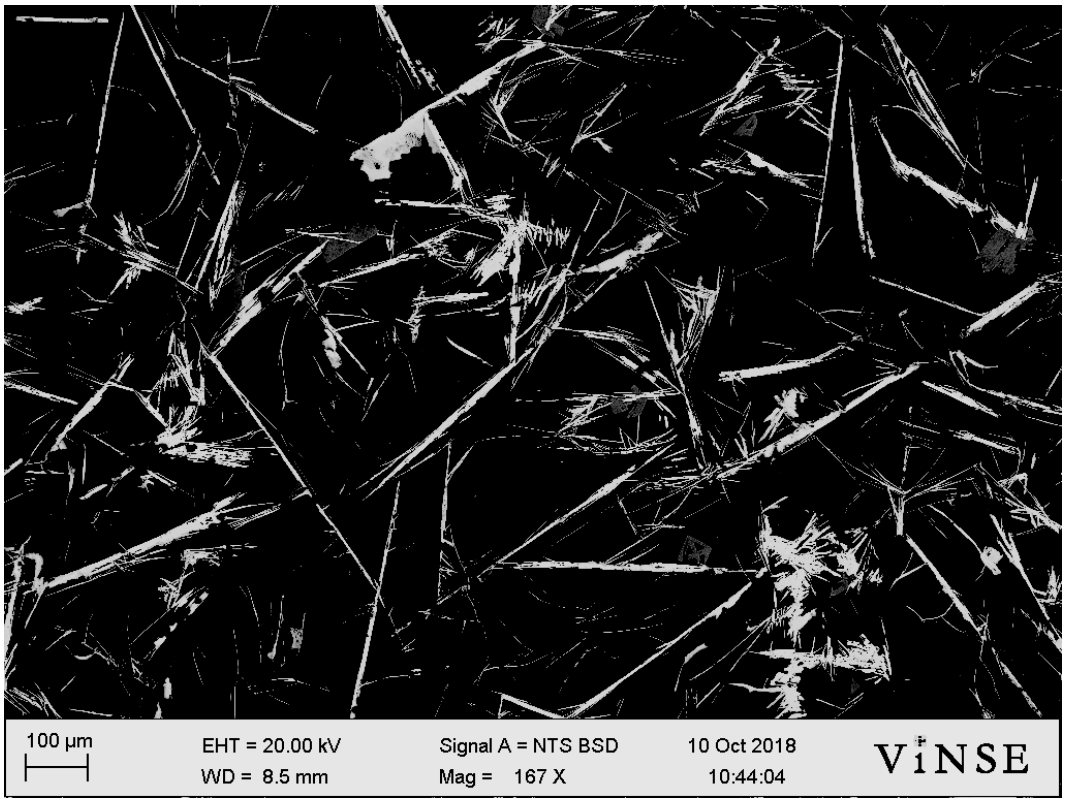

Figure 19. BSD Image 2, T4 Heat Treat (Area 2)

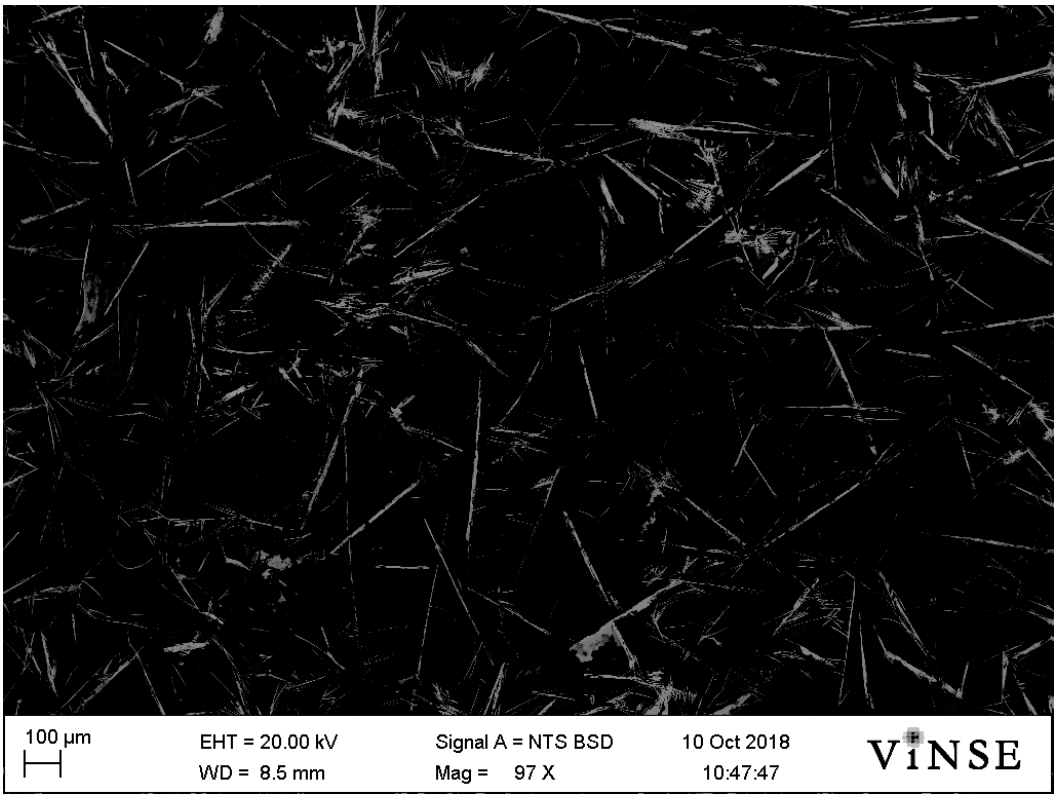

Figure 20. BSD Image 3, T4 Heat Treat (Area 3)

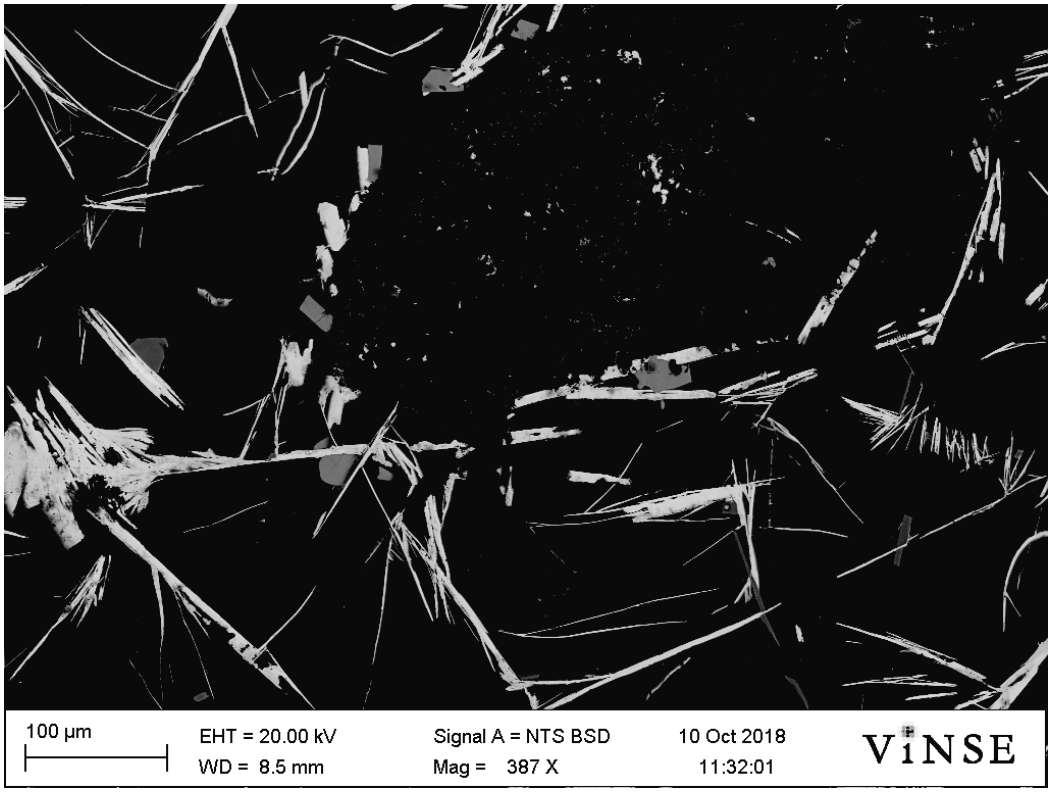

Figure 21. BSD Image 4, T4 Heat Treat (Area 4)

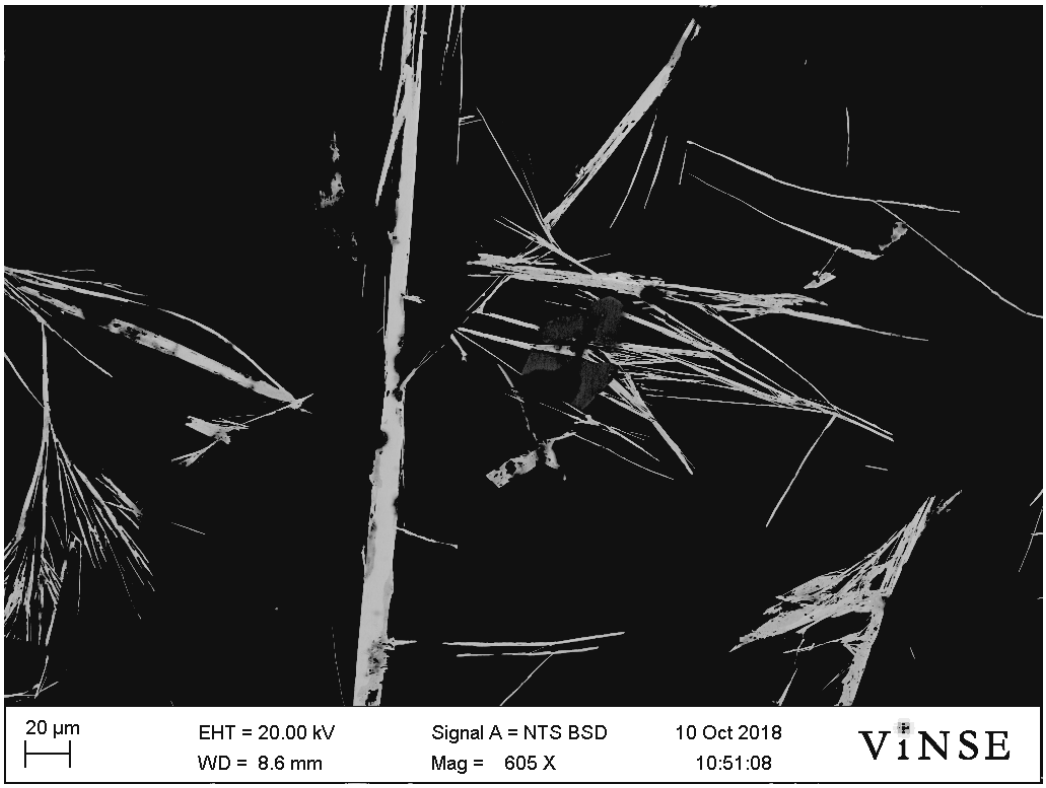

Figure 22. BSD Image 5, T4 Heat Treat (Area 5)

Figure 23. BSD Image 6, T4 Heat Treat (Area 6)

Figure 24. BSD Image 7, T4 Heat Treat (Area 7)

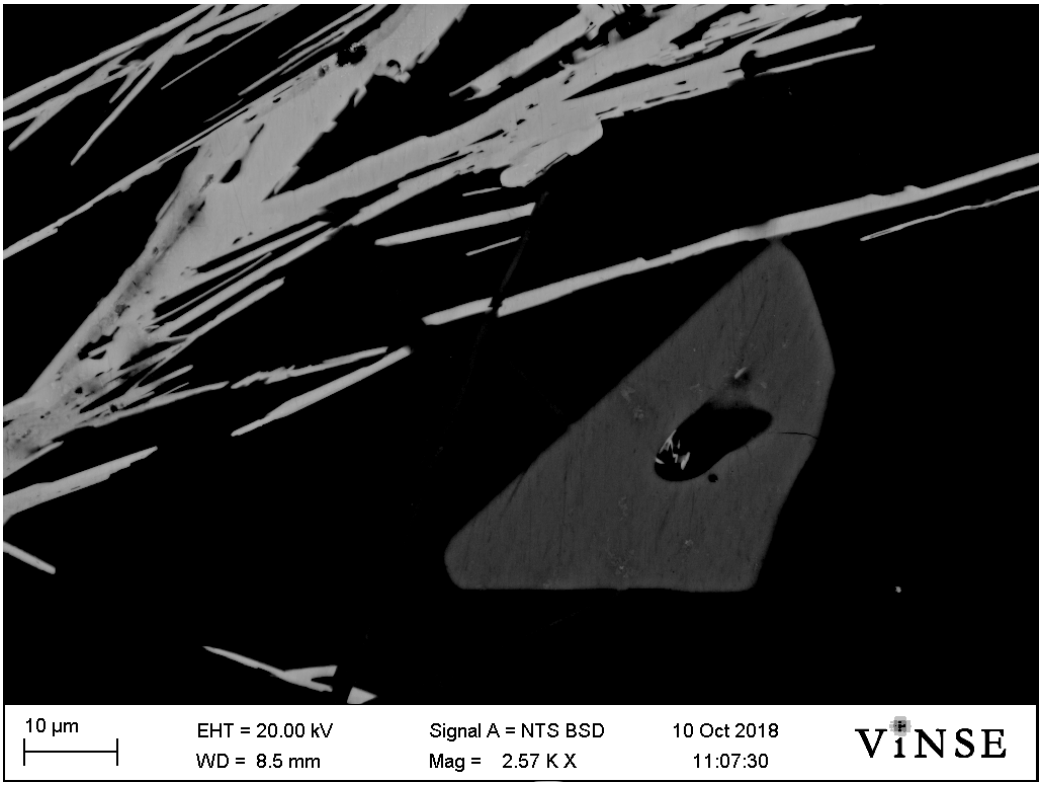

Figure 25. BSD Image 8, T4 Heat Treat (Area 8)

Figure 26. BSD Image 9, T4 Heat Treat (Area 9)

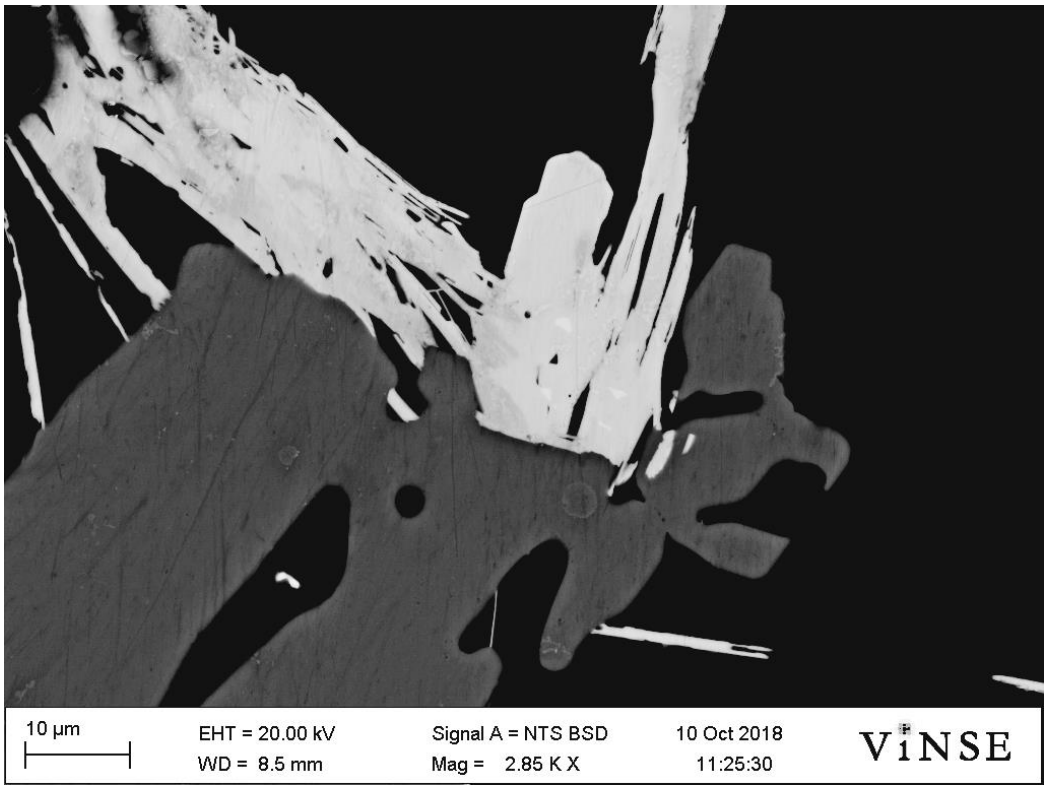

Figure 27. BSD Image 10, T4 Heat Treat (Area 10)

3.2.3 EDS Mapping and Intermetallic Composition Analysis

Once images had been obtained by the HE-SE2 and BSD, the x-ray detector was implemented to obtain EDS (energy dispersive x-ray spectroscopy) maps highlighting the elemental composition of the alloy. EDS was additionally used to take point ID spectra on all of the prevalent intermetallic compounds visible in the sample, allowing their compositions to be approximated using the atomic percentages reported by the program. Below, Figures **28-30** display three different areas of the sample under the HE-SE2 detector and the corresponding composite and individual elemental mapping from EDS.

From the EDS, Al, Si, Ce, Mg, O, Cu, C, and Fe can be seen dispersed throughout the alloy in varying concentrations. Carbon, while present, is mostly gathered in places where there are voids on the surface and was thus concluded to not be part of an intermetallic compound but rather contamination from polishing and prepping the sample. The same conclusion was drawn for oxygen; since it is mostly present in the relieved areas of the sample surface it is likely leftover from polishing.

In the individual and composite maps, clusters of cerium and copper are seen with minimal aluminum concentration. Magnesium and iron are fairly evenly dispersed throughout the sample, although there seem to be a few instances of higher magnesium concentration near surface voids. Iron is presumed to have either been a result of contamination from iron casting molds or added during the casting process as it was not directly reported as an alloying element for this material. Silicon appears to be concentrated in small, linear intermetallic compounds that are evenly distributed through the alloy. Aluminum is heavily concentrated across the sample surface (as anticipated) with the exception of the areas with high density of cerium and copper.

To approximate the chemical formulas of the intermetallic compounds in the sample, the point ID function of the EDS software was utilized. With this function, spectra can be taken for user-defined points on the sample surface; eighteen separate points were selected where intermetallic compounds appeared to exist. On each of these points, atomic percentages of each element present were estimated by the program. **Figure 31** and **Figure 32** show the secondary detector images and the points (Spectrum 6 – Spectrum 23) which were analyzed. **Table 3** shows the reported atomic percentages as well as the corresponding approximation of the compound compositions based on stoichiometry. The spectra output by the EDS software for each point can be found in the Appendix (Figures **48-65**).

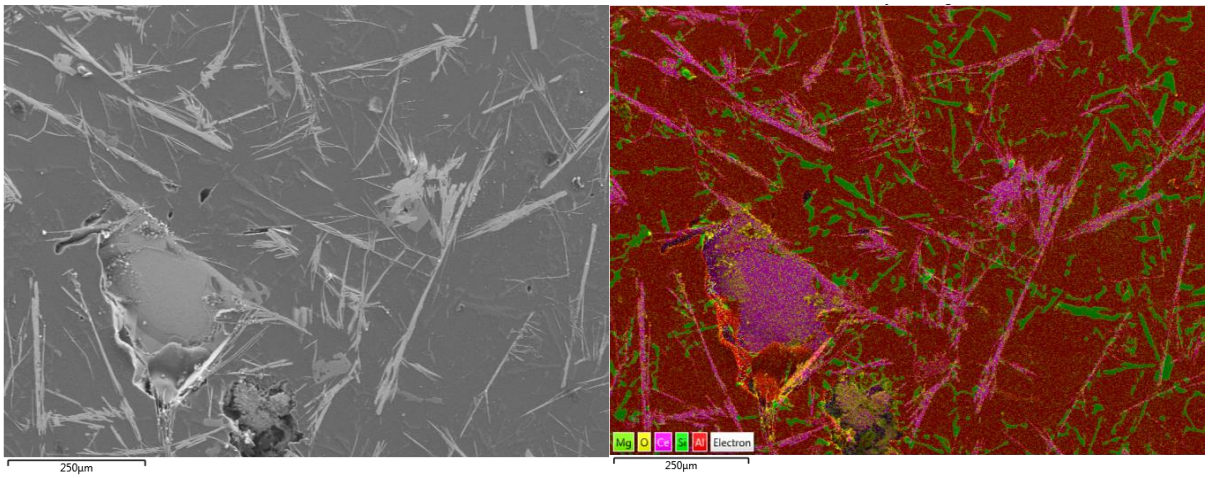

Figure 28. HE-SE2 Image 1 and Corresponding EDS Maps

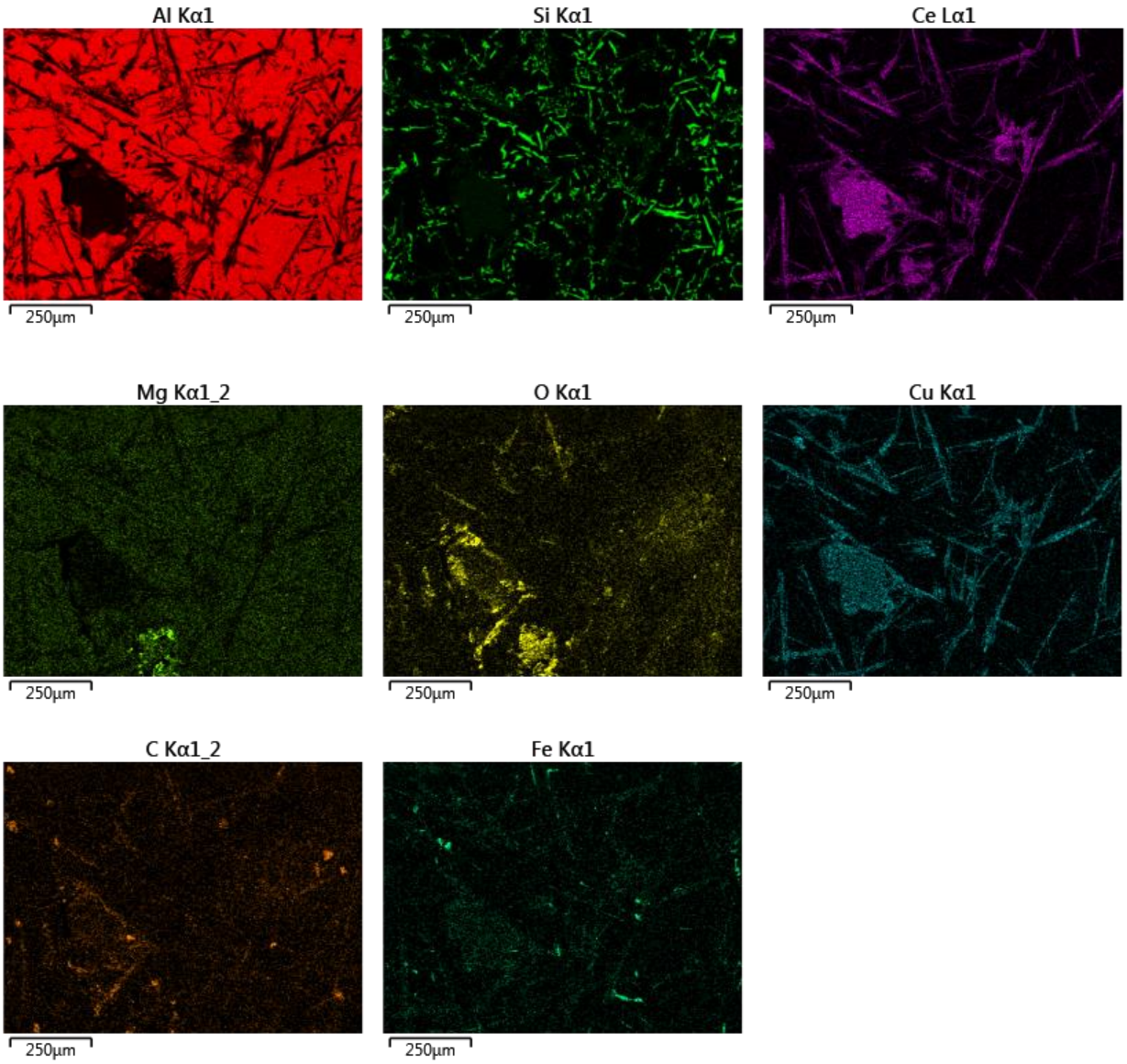

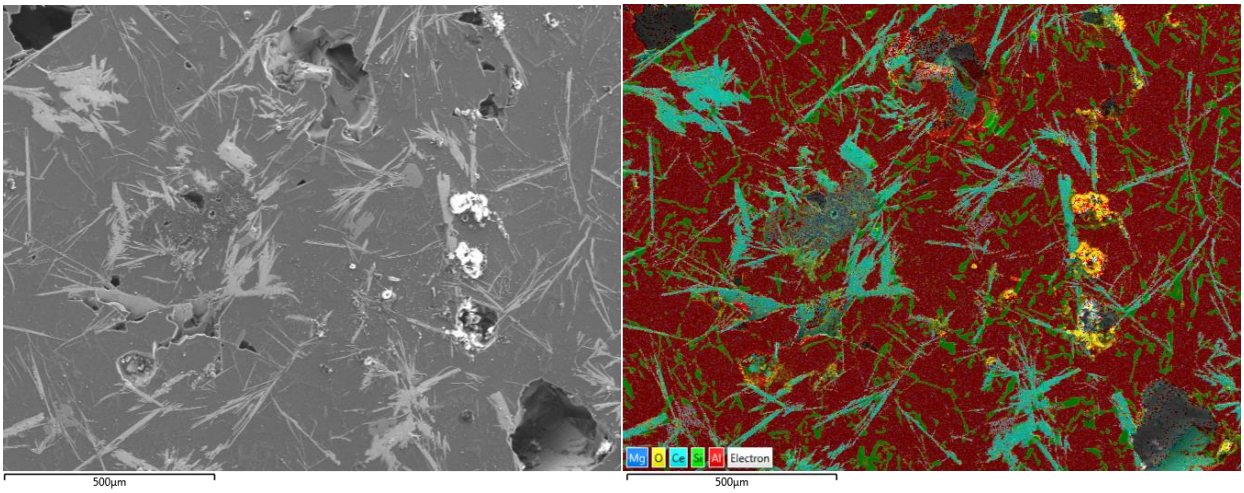

Figure 29. HE-SE2 Image 2 and Corresponding EDS Maps

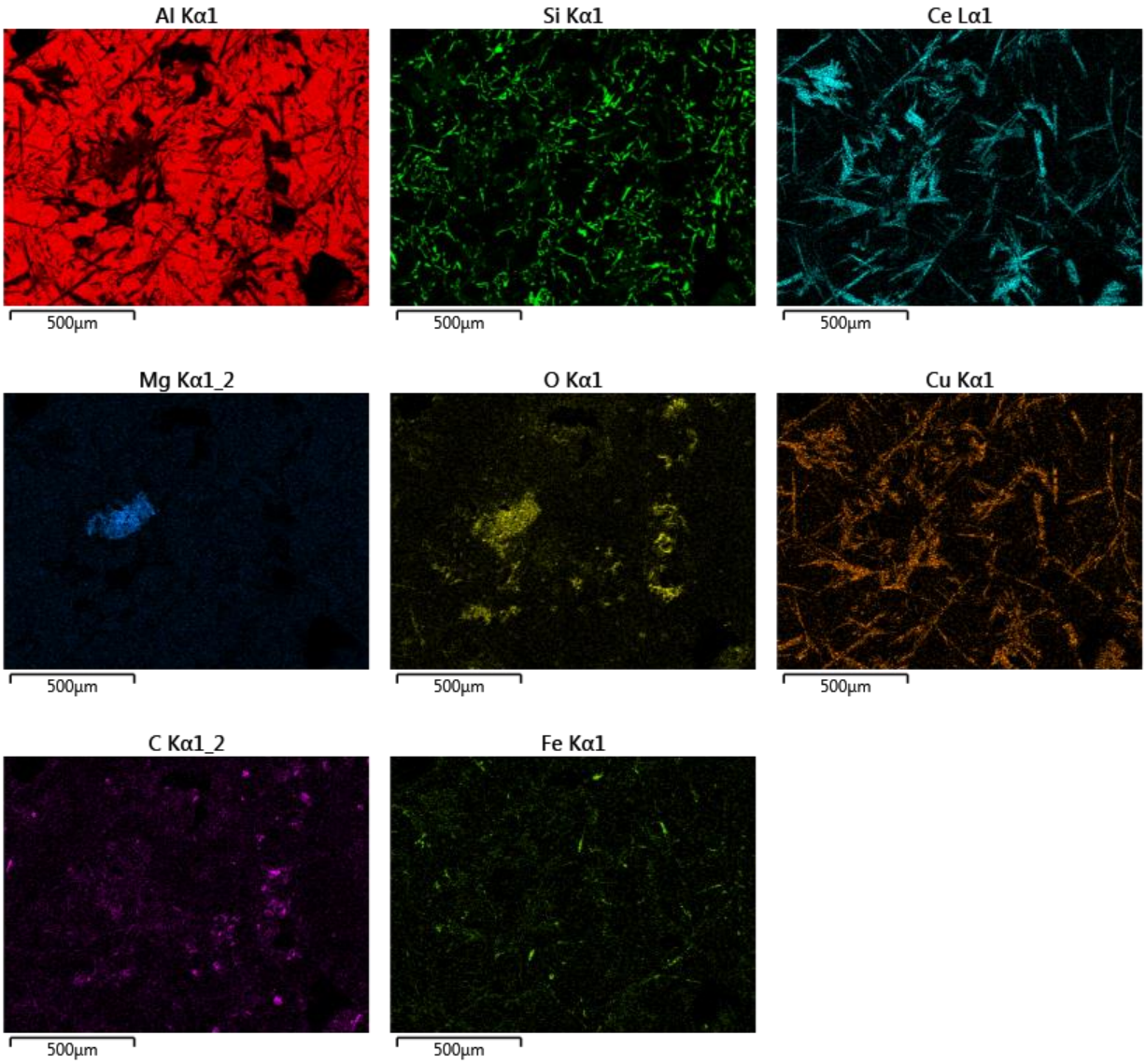

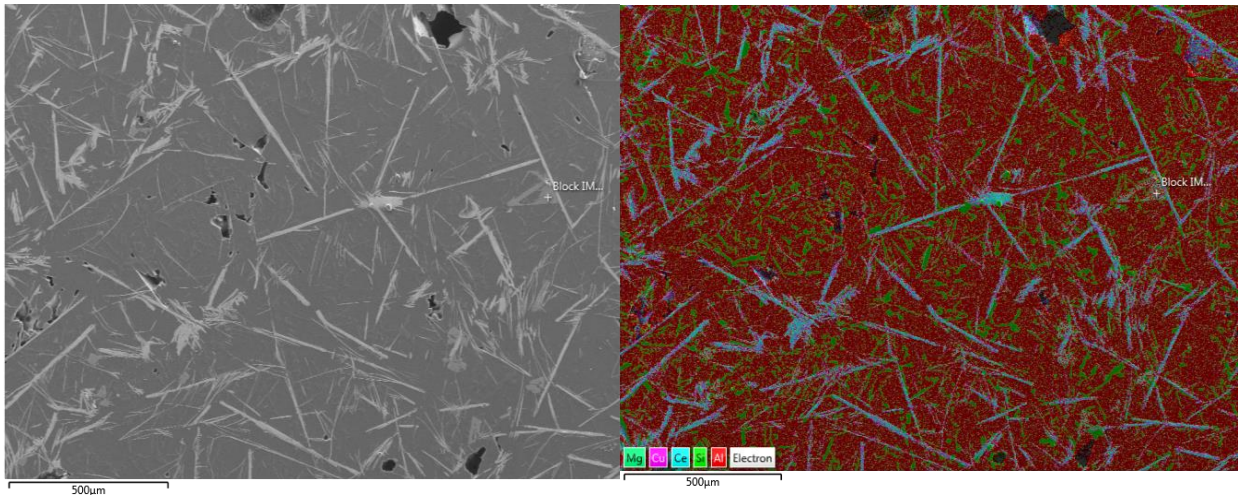

Figure 30. HE-SE2 Image 3 and Corresponding EDS Maps

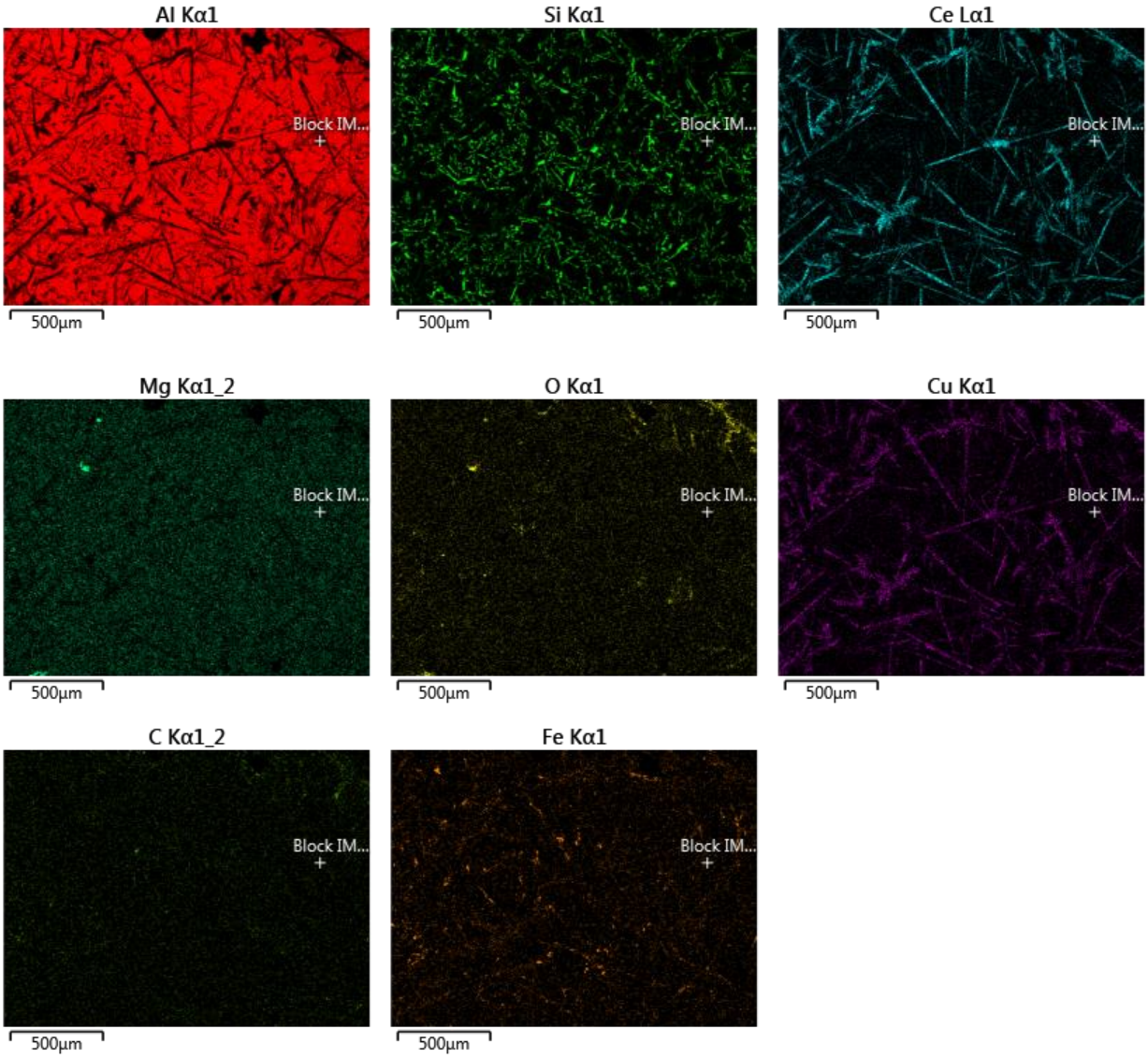

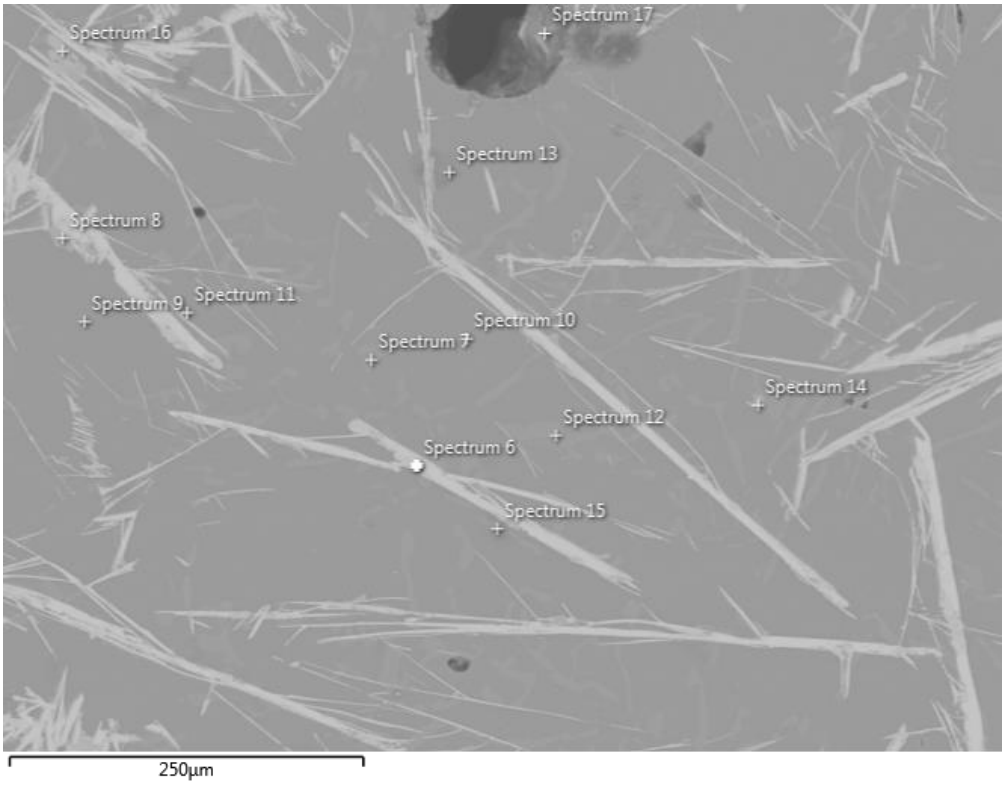

Figure 31. HE-SE2 Image 1 showing Point ID spectra (6-17) locations

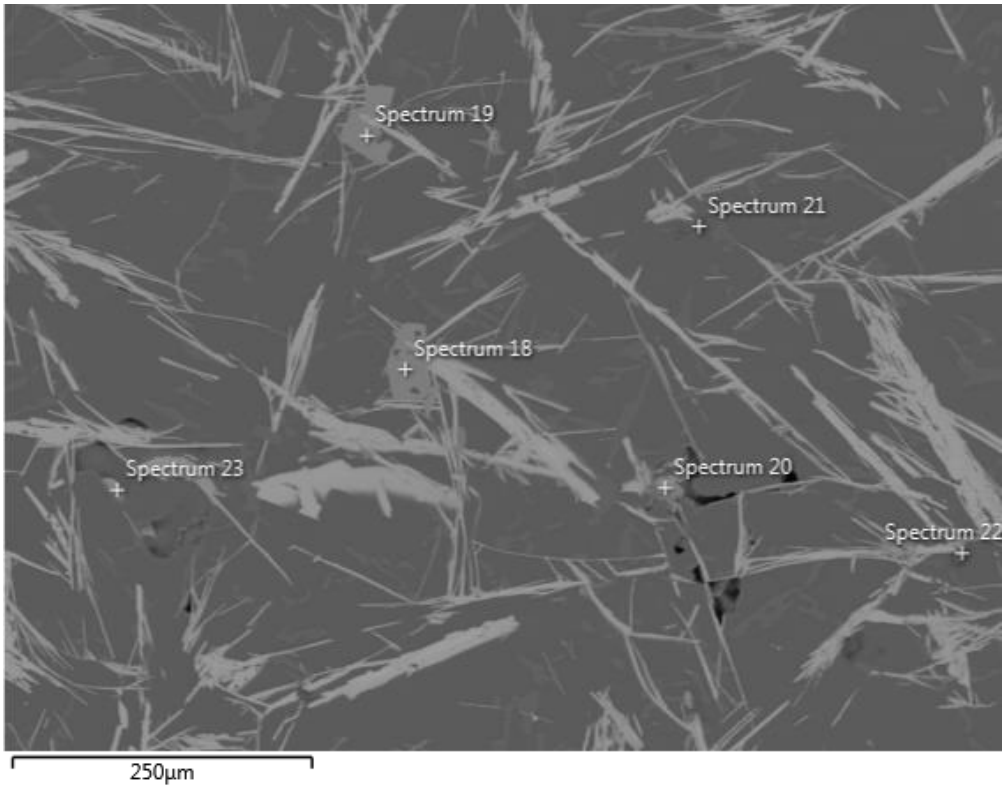

Figure 32. HE-SE2 Image 2 showing Point ID spectra (18-23) locations

Table 3. Atomic percentages and corresponding approximate intermetallic compositions

Spectrum	Al at. %	Ce at. %	Si at. %	Cu at. %	Mg at. %	O at. %	Fe at. %	Ti at. %	Zn at. %	Composition (approx.)
6	34.39	18.17	26.75	10.71	0.06	9.67			0.25	$Al_4Si_3Ce_2Cu$
7	3.19		95.81	0.10	0.01	0.90				$AlSi_{32}$
8	71.59		11.83	1.11		2.58	12.89			Al_7SiFe
9	94.31		0.99	0.26	0.38	3.84		0.06	0.16	Al matrix
10	94.96		1.03	0.26	0.34	3.16	0.05	0.05	0.16	Al matrix
11	64.36	0.05	0.69	0.21	0.20	34.30	0.04		0.15	Al matrix*
12	1.06		97.94	0.11	0.01	0.84			0.04	$AlSi_{98}$
13	87.18		1.20	0.28	0.33	10.77		0.08	0.16	Al matrix
14	47.97	6.05	10.49	10.81	0.91	23.23	0.32		0.21	Al_5SiFe
15	7.34	0.05	65.91	0.11		26.57			0.02	$AlSi_{10}$
16	81.78	4.07	2.07	0.53	1.94	1.59		7.66	0.36	$Al_{40}SiCe_2Ti_4Mg$
17	68.41	2.71	2.67	0.32	1.74	18.02		5.08	0.29	$Al_{56}Si_2Ce_2Ti_4Mg$
18	81.85	4.13	1.94	0.48	1.78	1.67	0.01	7.76	0.38	$Al_{40}SiCe_2Ti_4Mg$
19	81.58	4.13	2.03	0.43	1.78	1.84		7.83	0.38	$Al_{40}SiCe_2Ti_4Mg$
20	45.31	11.85	3.37	25.96		11.15	1.83		0.53	$Al_{30}Si_2Ce_8Cu_{17}Fe$
21	1.02	0.05	95.05	0.12	0.04	3.67			0.05	$AlSi_{95}$
22	6.40	0.11	73.20	0.13	0.15	19.92	0.03	0.05		$AlSi_{11}$
23	47.61	9.35	14.27	8.78	0.11	18.68	0.99		0.21	$Al_{10}Si_3Ce_2Cu_2$

**Oxygen determined to be present as a result of polishing and thus not included in intermetallic formula*

As can be seen by **Table 3** above, there are numerous intermetallics formed in this alloy with similar atomic elements but vastly different stoichiometric ratios. It is important to note that while the spectra obtained by the EDS reflects the composition of the point selected, the data comes from the entire penetration volume of the x-rays and not just the surface of the specimen. Elements reported in trace amounts (<1%) as well as contaminating elements present from polishing (oxygen) are almost certainly not present in the intermetallic compound being analyzed, but show up from x-rays penetrating the bulk material and interacting with surface inclusions.

Intermetallic formulas calculated for each spectrum are shown and color coded to indicate those which are suspected to be the same compound based on similarities in appearance and calculated formula. Slight differences in stoichiometric ratio are likely caused by the aforementioned contamination of data from the penetration volume. Four of the points measured were determined to be the aluminum matrix (Spectra 9-11 and 13), while the remaining compounds had varying concentrations of Si, Cu, Ce, Fe, Ti, and Mg. Titanium, while not reported in the alloy composition by Eck Industries, is expected to have been included as an alloying addition during

casting as the reported concentration cannot be dismissed as noise or error. As mentioned earlier in this section, iron is expected to be a result of contamination from using cast iron molds.

3.3 FSW Results

3.3.1 Bead on Plate Welding

Before attempting butt welds, two two-inch wide pieces of the alloy were cut and surfaced to be used for bead on plate (BOP) welding. Bead on plate welding in FSW refers to running the tool through a flat plate of the material in the same fashion as would be done for a typical FSW joint. Through manipulation of the weld parameters, an initial idea of what settings are required to produce a high surface quality and consistent consolidation can be attained.

With the current experimental setup in the lab, the minimum width able to be clamped down for a weld with adequate security is two inches. Only two pieces were cut to save the majority of the material for butt welding. BOP welds were conducted slightly off-center so that there would be enough space to complete a second pass on the other side, and were additionally welded on both the top and bottom surface to collect additional data. Since the material is thicker than is typically used for FSW (1/2-inch vs. 1/4-inch), there was enough unaffected material beneath the surface of the initial BOP welds that this was a logical way to try and maximize the BOP results.

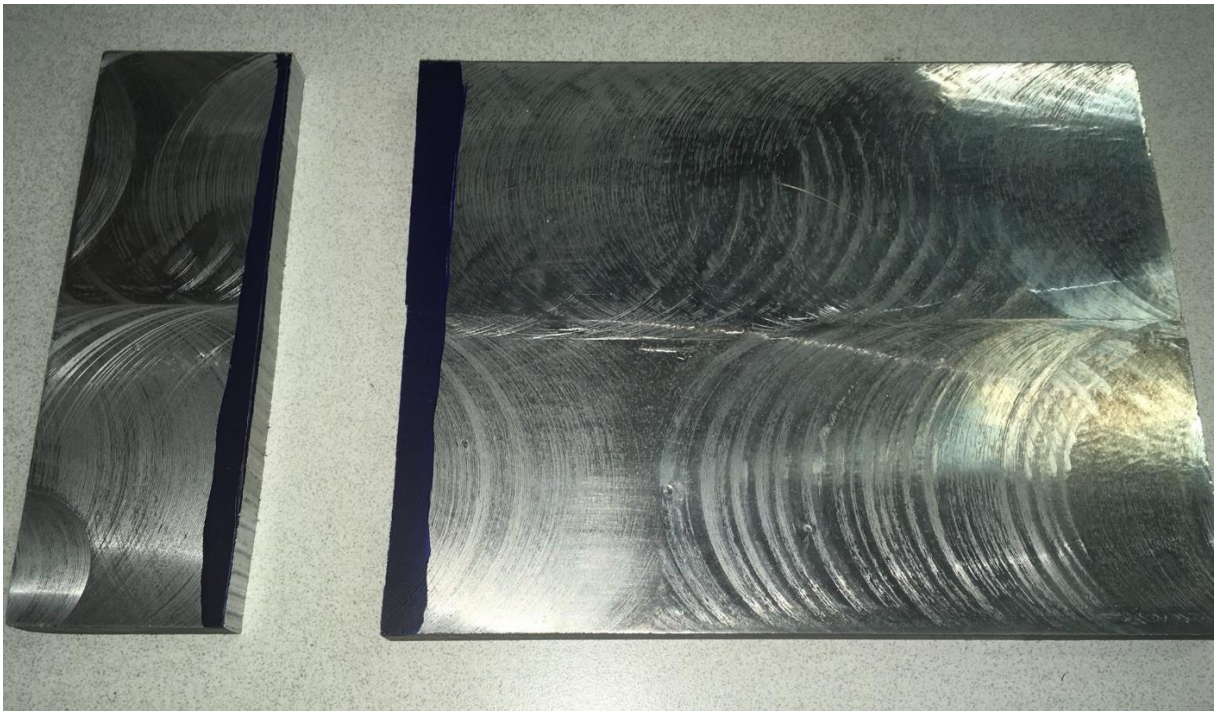

Figure 33. Surfaced and cut Al-10Si-7Ce-4.3Cu-0.4Mg base plate (6-inch by 10-inch); left piece demonstrates size of pieces utilized for BOP welding

Figure 33 shows what the 6-inch by 10-inch plate looked like after surfacing and shows one of the cut two-inch pieces used for BOP welds. The additional 6-inch by 6-inch plate provided by Eck Industries was also surfaced but the material was saved for use in friction stir butt welding. A table showing all of the FSW parameters used in the following BOP weld trials is shown below in **Table 4**.

Table 4. BOP Welding initialized parameters, trials 02-16

Trial	Spindle RPM	Traverse Rate (IPM)	Plunge Depth (inches)
02	600	6.0	0.205
03	600	5.5	0.205
04	750	6.0	0.205
05	800	6.0	0.210
07	800	6.0	0.210
08	800	6.0	0.210
09	800	6.0	0.215
10	800	6.0	0.220
12	800	1.0	0.215
14	900	6.0	0.215
15	1000	6.0	0.220
16	1000	6.0	0.215

Figure 34. BOP Welding, runs 02-05

To begin bead on plate welding, initial weld parameters of 600 rpm, six inches per minute (IPM) traverse, and 0.205 inch plunge depth were selected. This trial can be seen in **Figure 34**, labelled 02. The surface quality of this weld was initially promising, but was cancelled prematurely

by the machine due to exceeding XY force limits. To combat this, the traverse for the following run was decreased to five and a half IPM, but again the weld was stopped due to XY force limits (trial 03). Based on the surface quality, it was hypothesized that there was insufficient energy deposition to plasticize the material. To combat this, the traverse was returned to six inches per minute and the RPM was incrementally increased for the following two trials, 04 and 05. While 750 RPM still resulted in poor mixing, the quality improved greatly once the RPM was increased to 800 and the plunge depth was slightly increased to 0.210 inches for trial 05 (see **Figure 34** above). The parameters for trial 05 gave promising initial results; the surface quality was greatly improved and no alarms were set off by the machine, allowing the weld to complete the entire traverse. While there is a void seen on the retreating side, this is suspected to partially stem from the fact that the material on this side had already been mixed and disturbed by the previous bead on plate passes. It also appears that the shoulder did not reached full engagement with these parameters.

In order to determine if the parameters from trial 05 were a good selection or not, the same parameters were selected for the following run, trial 07. While the tool completed the entire traverse on trial 07, there was low shoulder engagement across the length. After the weld, it was speculated that the tool may not have been fully secured in the holder, which could have potentially caused the drop in engagement. Prior to trial 08, the tool was re-secured with an axial force keeping it tightly placed in the holder and the run was then conducted at the same parameters again. After a few inches of welding, it was determined that the engagement was still low and that there was a wormhole forming. The weld was stopped early, and the plunge depth was increased to 0.215 inches for trial 09 (see **Figure 35**). This trial showed decent surface quality, but still did not display full engagement of the tool shoulder. These three runs, although conducted at very similar settings, had significantly different results. This demonstrates the narrow process window in which this particular alloy seems to be friction stir weldable due to the various intermetallics. This will be further discussed in Chapter 4.

The next run conducted, trial 10, can also be seen in **Figure 35**. The plunge depth was increased to 0.220 inches in an attempt to get rid of the engagement issues, but the results were even worse than previous attempts and the weld displayed ragged surface quality and a visible wormhole. In order to determine if there was wobble or a misalignment affecting the engagement issues, trial 12 was conducted as an edge pool weld to observe how the tool was engaging at the

surface as it entered the material. Significant wobble and consequent misalignment of the tool in the material was seen. Prior to next BOP welds, Ph.D. candidate and lab mate Adam Jarrell corrected runout along the tool column of the machine to prevent further issues.

Figure 35. BOP Welding, runs 07-12

With runout issues resolved, it was also hypothesized that an increase in RPM would be helpful in increasing the engagement of the tool shoulder. Trial 14 was run at 900 RPM and six IPM traverse, but displayed low engagement and was stopped early; trial 15 was then conducted at 1000 RPM, six IPM traverse, and a slightly increased plunge depth of 0.220 inches (see **Figure 36**). This weld showed the best surface quality, but still had a small wormhole void which likely resulted from the overlapping with the previous BOP weld. The best results obtained in all of the BOP welds were the results of the following weld on a fresh side of the material, trial 16 (see **Figure 37**); this weld was conducted at 1000 rpm, at 0.215 inches plunge depth and six IPM traverse. The engagement issues have almost been eliminated in this weld, and there is better surface quality.

Figure 36. BOP Welding, runs 14-15

Figure 37. BOP Welding, run 16

Since the best BOP results were obtained at 1000 RPM, the same RPM was used in the following welds. In a last attempt to fully utilize the BOP plate material, the two pieces were surfaced flat on each side and then friction stir welded together. The same process was then repeated, but the weld was conducted on the opposite side of each piece in an attempt to weld on the least disturbed areas of the material (see **Figure 38** and **Figure 39**). The results were overall disappointing; trials 01-03 were conducted at a six-inch per minute traverse rate, and trials 06 and 07 were conducted at five-inches per minute. In all trials, the tool was rotating at 1000 RPM. Even

though these settings were similar to settings used on previous BOP welds that gave decent results, all of these welds showed insufficient mixing, low shoulder engagement and severe surface galling. It is theorized that the excessive manipulation of the BOP plates may have overworked the material and caused the properties to change; this would be possible through strain hardening or the heating of the plate during welding. [20] For the FSW trials on unused plates, parameters were initialized at 1000 RPM and 5 IPM traverse to observe if these were reliable parameters for FSW or not. A few of the FSW runs on the BOP plates were stopped early by the machine due to force limits; Adam Jarrell, Ph.D. candidate and graduate researcher in the VUWAL, programmed, tested, and implemented a torque controller onto the machine prior to the butt plate welds. This helped in avoiding force limits and over plunging.

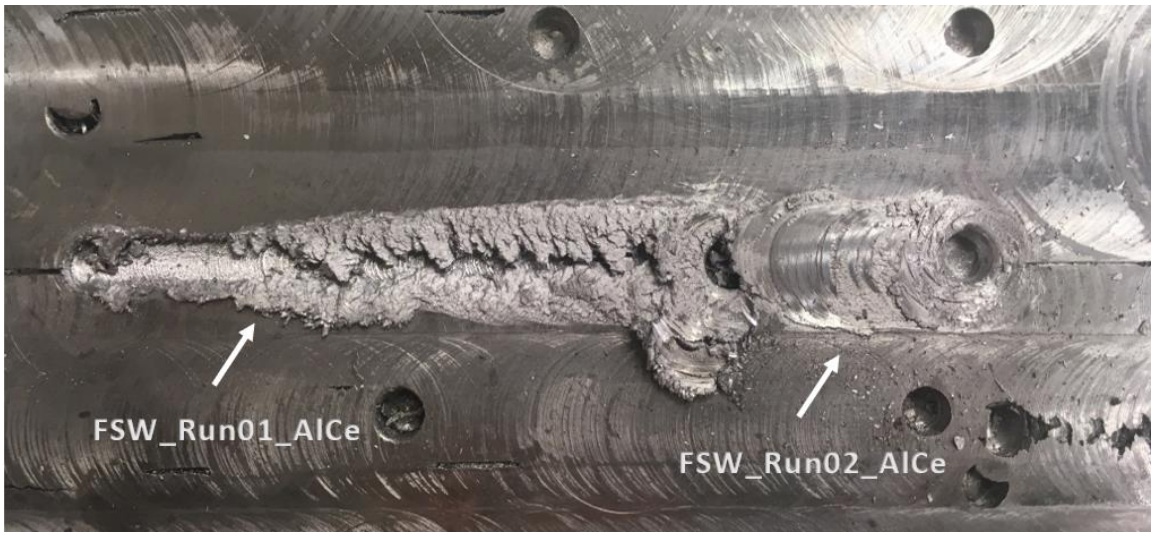

Figure 38. FSW of BOP pieces, runs 01-02

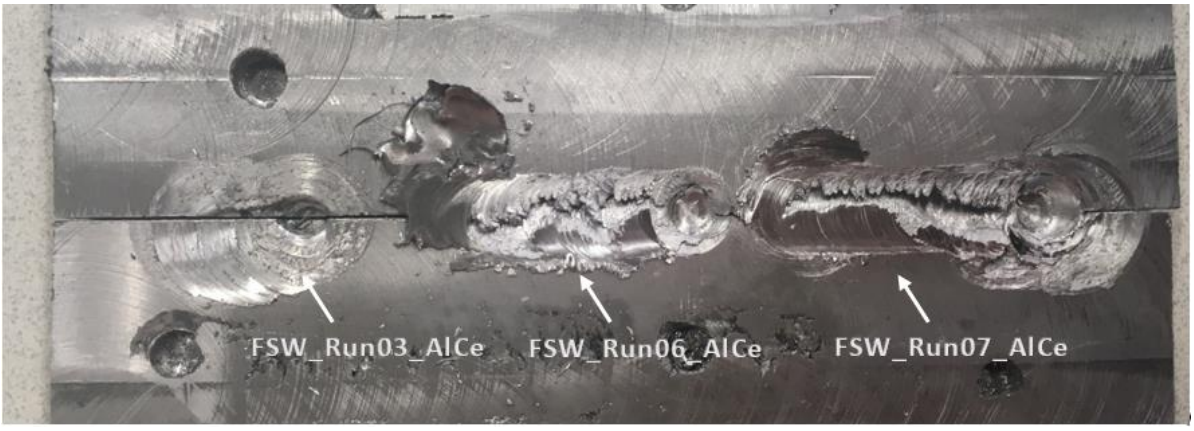

Figure 39. FSW of BOP pieces, runs 03-07

3.3.2 Butt Welding

Table 5 below outlines all of the initialized parameters for the butt welds in this section for convenience. In some welds, parameters were updated mid-process. Any updates made during welds will be discussed in the following text.

Table 5. FSW initialized parameters, Welds 1-7

Weld	Spindle RPM	Traverse Rate (IPM)	Plunge Depth (inches)	Torque Reference (Nm)
1	1000	5.0	0.205	15
2	1000	5.5	0.205	13
3	1000	3.0	0.205	15
5	1000	3.0	0.205	15
6	1000	3.0	0.205	17
7	1000	3.0	0.205	17

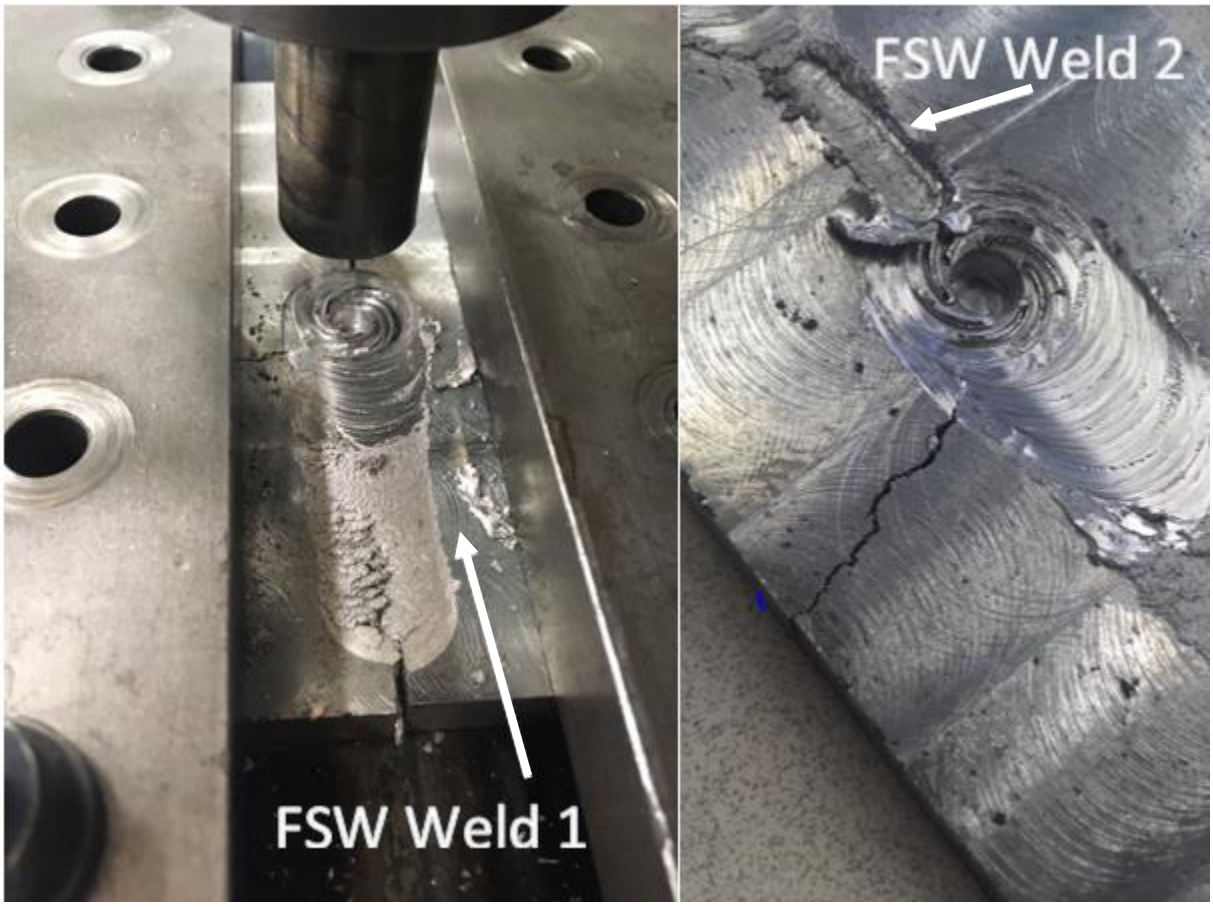

Figure 40. FSW, Welds 1 and 2 (upper right)

The alloy pieces used for friction stir welding all had widths of approximately one and a half inches. The first friction stir weld, Weld 1, was conducted at the parameters that provided the best results in the BOP welding trials: 1000 RPM, and five IPM traverse. It can be seen in **Figure 40**. The data for the best BOP run, trial 16 (**Figure 37**), was additionally analyzed to determine what torque value would be best to input for the new torque controller. It was determined from this dataset that 15 Nm would be a good initial value to aim for. If the torque readings during welding are showing values exceeding the torque limit set by the user, the table will be lowered in small steps by the torque controller until it is back in the appropriate bounds. As Weld 1 began, it could clearly be seen that there was insufficient stirring and that the material did not appear to be fulling plasticizing; to increase the heat deposition, the traverse was lowered from five IPM to three IPM, and a much higher quality weld began to appear. Unfortunately, the tool became stuck after an inch or so of welding and is suspected to have over plunged. The tool had to be pulled out manually. Later, a large crack developed (see **Figure 40**) stemming from where the tool was pulled from the weld, demonstrating the brittleness of the alloy. Weld 2, which was run at 1000 RPM, three IPM traverse, and 13 Nm torque, showed very poor shoulder engagement and virtually no mixing or welding at all. From this, it was determined that the torque must need to be higher than 13 Nm (at minimum 15 Nm, or also run at a lower traverse rate) for sufficient plasticization.

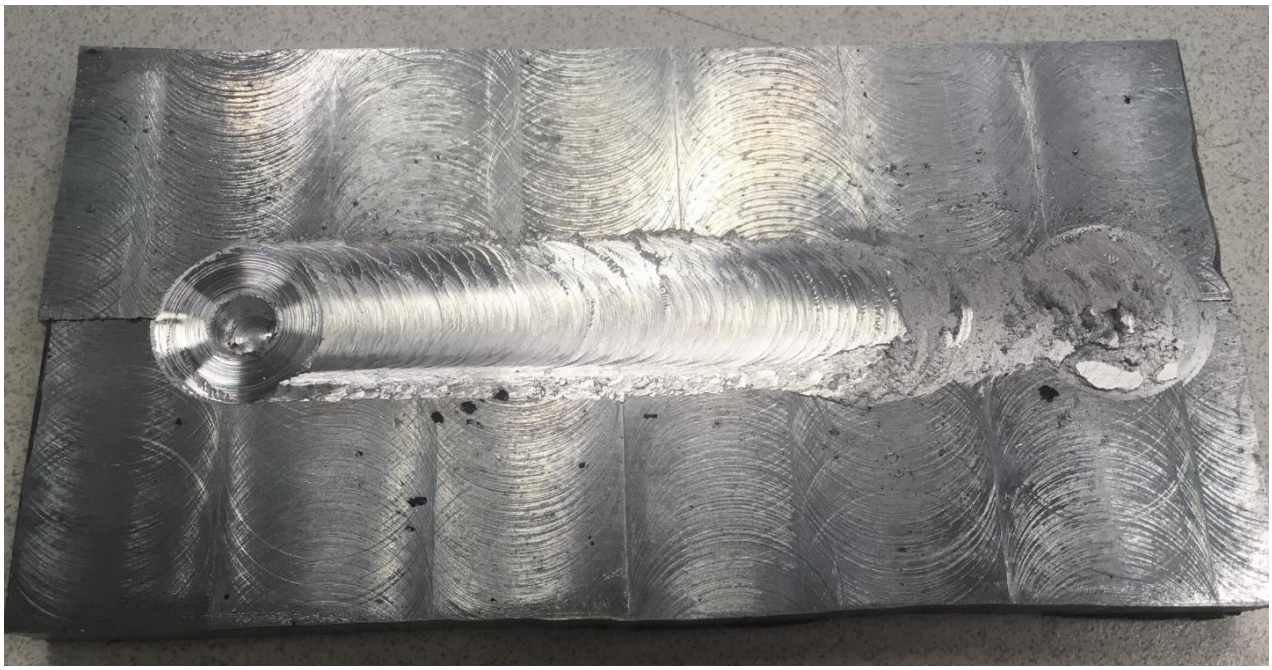

Figure 41. FSW, Weld 3

The subsequent FSW was started at the same parameters that yielded an inch of fair results on the previous weld. **Figure 41** displays Weld 3, which was the highest quality friction stir weld of the material produced. The weld was initialized at 1000 RPM, three IPM traverse and 15 Nm torque, but when there was insufficient mixing an inch or so into the weld the torque was increased to 16 Nm and the weld quality improved greatly. The surface showed consistent shear bands and engagement with the tool shoulder. This weld provided enough viable friction stir welded alloy for tensile tests and microstructural analysis, which will be discussed in sections 3.3.3 and 3.3.4.

The results for the following welds, runs 5-7 (see **Figure 42** and **Figure 43** below), were unfortunately not as high quality. All welds were run at 1000 RPM and three IPM traverse; Weld 5 was started at 15 Nm torque but was showing low engagement after an inch or so of welding and the torque was updated to 17 Nm. The quality was slowly beginning to improve but the plunge depth limit of the machine was reached because of the high torque causing the weld to stop early. The following weld, Weld 6, had the exact same issues. Weld 7 was run at the same parameters (17 Nm torque), but in this run the axial force was actually significant enough to cause the plates to split, ruining the welding results. Adequate plasticization was at least observed on the surface, indicating that if splitting had not occurred the weld may have been successful.

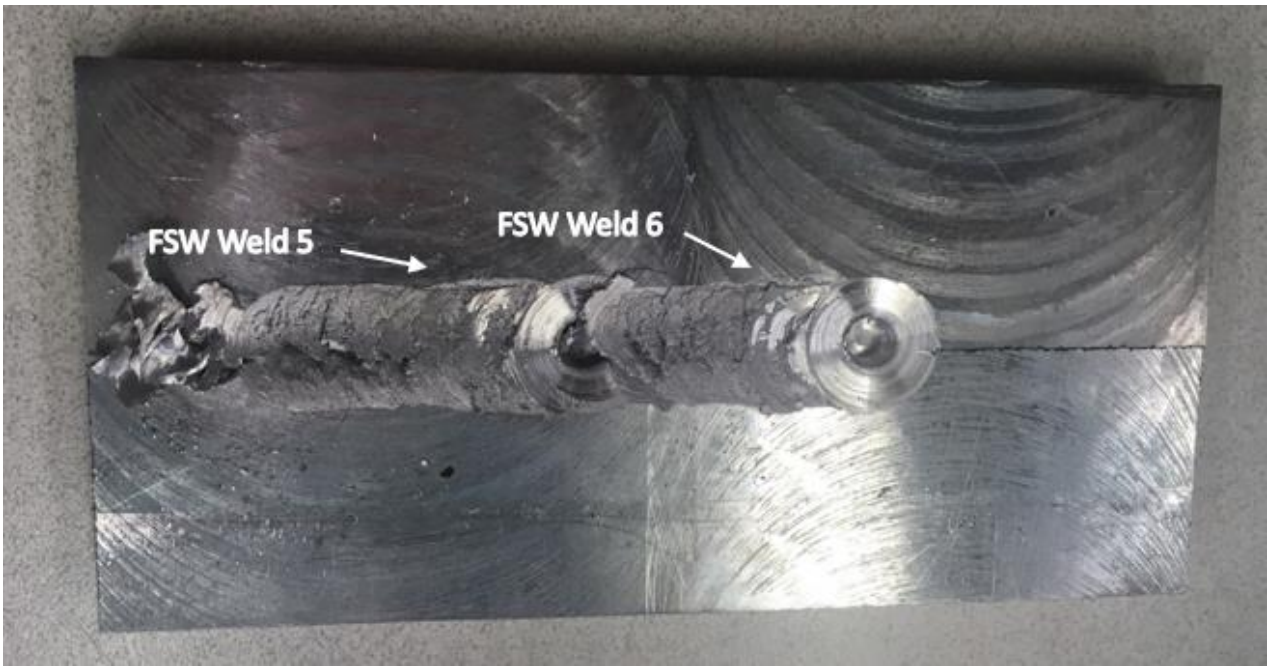

Figure 42. FSW, Welds 5 and 6

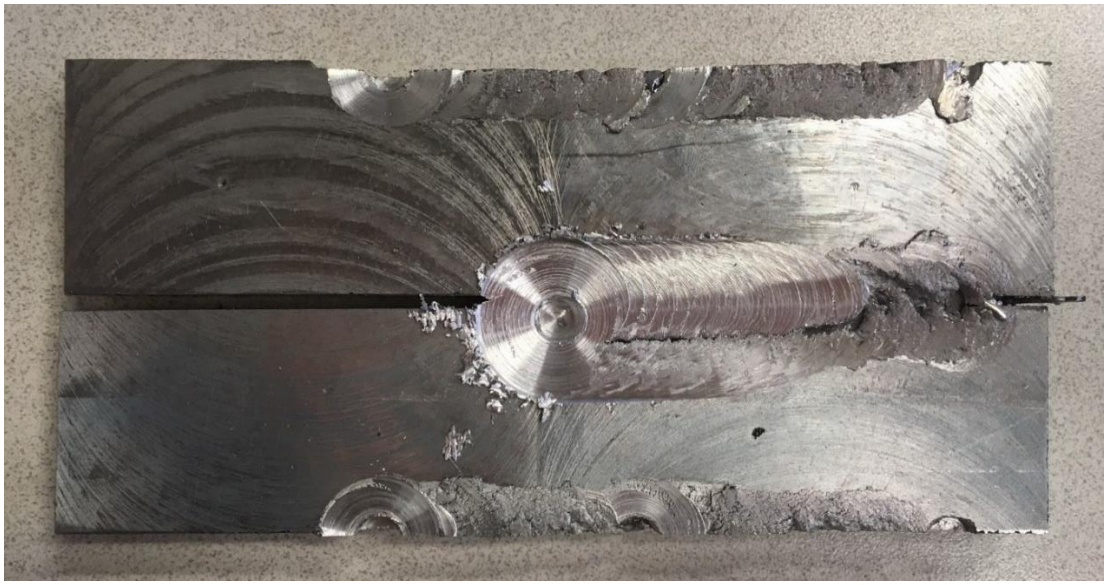

Figure 43. FSW, Weld 7

3.3.3 Post-Weld Microstructural Analysis

While the majority of the welded material from Weld 3 (**Figure 41**) was utilized to machine substandard tensile bars (discussed in section 3.3.4), a small cross section was cut away to be polished, etched, and then imaged under the optical microscope. This piece was approximately 1/4-inch thick. After the cross-sectional surface was wet-sanded down to 1-µm surface refinement, a potassium hydroxide etchant was used to highlight the intermetallic compounds in the weld zone, the thermo-mechanically affected zone (TMAZ), and the non-welded zone. **Figure 44** displays optical microscope images that were obtained at the bottom and to the right of the weld nugget.

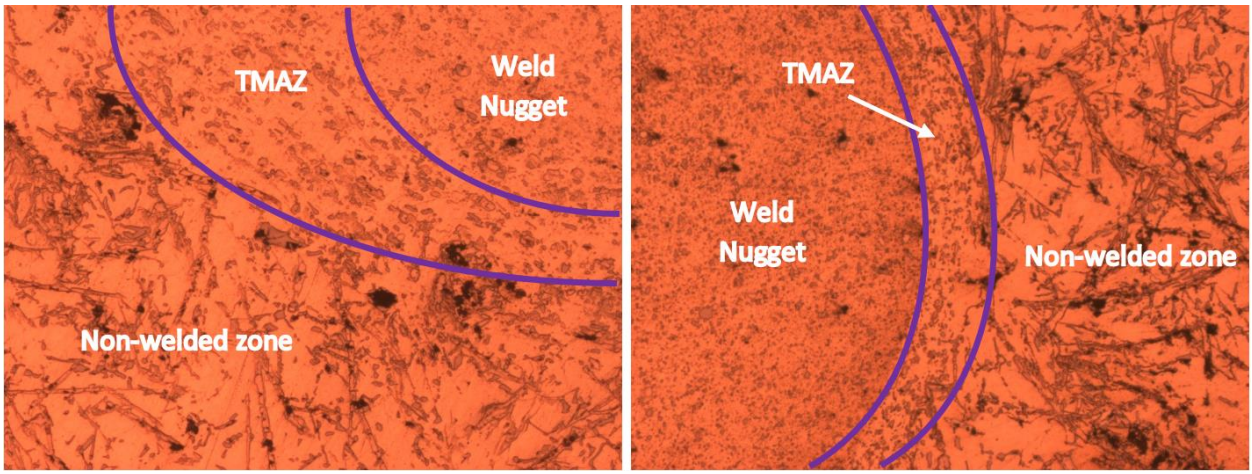

Figure 44. Optical microscope image of etched FSW cross-section, left and underneath the nugget (left) and to the right of the nugget (right), 5x magnification

Most clearly visible in these images is the intermetallic compound that is large, linear and scratch-like in appearance; this compound is known to have a composition somewhat resembling $Al_4Si_3Ce_2Cu$ based on the data obtained by the EDS in section 3.2.3 (**Table 3**). These intermetallic compounds (as well as the other smaller ones that can be discerned from the image) are in an undisturbed state in the non-welded zone, but become stretched in the thermo-mechanically affected zone and then break into finer pieces in the weld nugget. This lines up with expected results as the most significant stirring would happen close to the tool pin; the more stirring experienced by the material, the more the intermetallic compounds would be broken up and dispersed throughout the aluminum matrix. The compounds also appear to be prone to cracking, as there are voids seen on the surface throughout the images and particularly on the intermetallics.

This can also be seen clearly in the close up optical microscopy images of the intermetallic

compounds in each of these zones (see **Figure 45**); although all of these images were taken at 50x magnification, the largest intermetallic compound visible in the TMAZ showed an approximate 50% reduction in size as compared to the non-welded zone, and can be seen broken up and stretched around the weld nugget. The various compounds seen around the intermetallics are then seen even further reduced in size and dispersed in the 50x magnification image of the intermetallic compounds in the weld nugget.

In addition to the intermetallic dispersal, it was observed that the apparent boundary between the two aluminum cerium plates when they were clamped together for welding is still visible through the images obtained by the optical microscope as seen in **Figure 46**. These images seem to imply that the material was only truly thoroughly mixed at and immediately outside the weld nugget for this weld. It should be noted, however, that the plates utilized for these welds were thicker than is typically used for friction stir butt welding, and thus it is assumed that with a more standardized plate thickness and perhaps a higher applied torque that full consolidation would be achieved all the way down to the joint base.

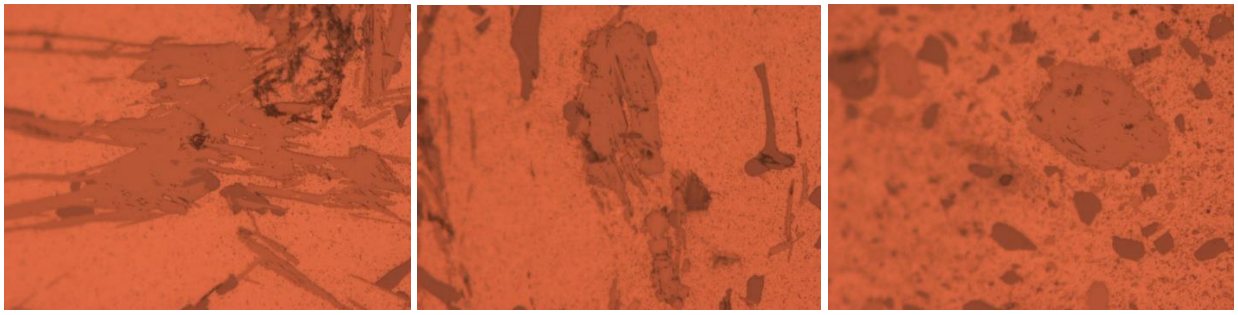

Figure 45. Close up of intermetallic compounds in the non-welded zone (left), the TMAZ (middle), and the weld nugget (right)

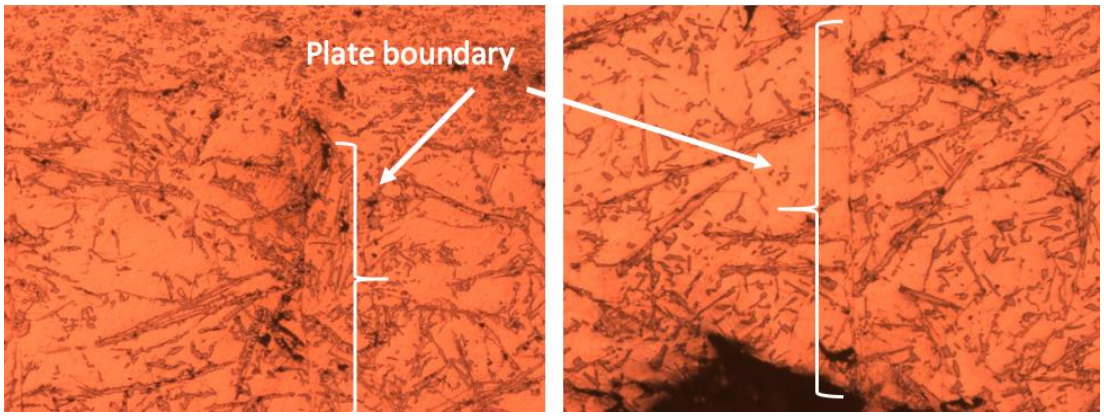

Figure 46. Optical microscope images taken at the base of the weld nugget (left) and at the bottom of the cross section where the two plates met, below the nugget (right)

3.3.4 Weld Tensile Tests

In order to determine the strength of the friction stir welded Al-10Si-7Ce-4.3Cu-0.4Mg alloy, substandard tensile bars were machined from cross-sectional cuts of the material on the best friction stir welded plate, Weld 3 (seen in **Figure 41**). A picture of one of the three tensile bars obtained from the good weld can be seen below in **Figure 47**; this is the maximum number that could be produced once cross-sectional material was removed for optical microscopy. The width is approximately 1/2-inch at the ends and tapers down to 1/4-inch in the middle, and the sample is 1/4-inch thick. Since the welded plate was originally approximately 1/2-inch thick, the sample was milled down to 1/4-inch thickness from the bottom side of the plate.

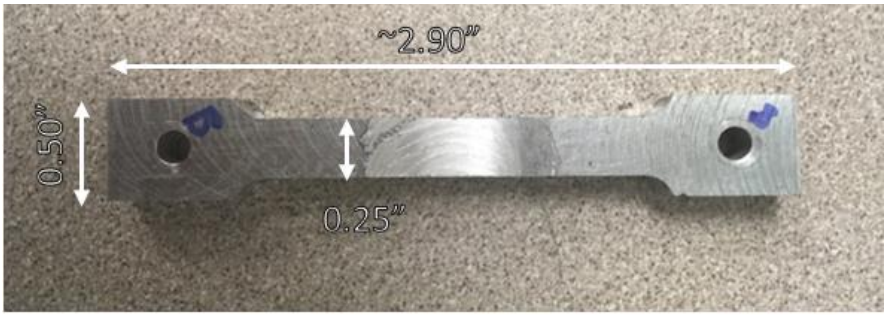

Figure 47. Tensile bars cut from FSW cross section (Sample B)

The extensometer was not able to be used for these tensile tests due to non-standard tensile bar sizes. Once the sample was secured in the clamps, there was not enough room for the extensometer to be attached between the jaws of the testing machine. Like the tensile bars of the parent alloy, the fracture surface from these failed samples displayed very brittle peaks and minimal elongation. The strength of the FSW tensile bars, although lower than the parent alloy, was still comparable to the parent alloy with ultimate tensile strengths of 2.9 kN, 3.2 kN, and 2.9 kN for samples A, B, and C respectively. The parent alloy had minimum and maximum UTS values of 2.7 kN and 4.0 kN, which supports the conclusion that the friction stir welded zone of a butt weld of this alloy has comparable strength to the base material.

4 Discussion

4.1 Friction Stir Weldability

Overall, the results in Chapter 3 display that while this alloy can be friction stir welded, the exact window of parameters in which these welds will be of sufficient quality is very small. From the BOP results seen in **Figure 37** and the high quality FSW seen in **Figure 41**, it can be concluded that an RPM of 1000 or higher will provide best mixing and surface quality. From the tests with the torque controller it as also observed that high axial force and torque (17 Nm or more) in combination with a slower traverse rate is critical to sufficient plasticization and mixing of the material. While some successful results were obtained in these tests, it is probable that attempting welds on similar aluminum cerium alloys would be much easier on a machine with higher force limits and a more secure clamping system for wide plates. The high strain rate required to achieve desired weld quality must be attained by having sufficient force from the tool shoulder to shear the material at the surface (which additionally provides localized heating). If the exact parameters were able to be more finely tuned to a process window on a friction stir welding machine with the capability to apply higher torque and axial force, it is likely that this material would be able to be welded somewhat reliably and consistently. In general, it is unique as it is more difficult to weld in regards to consistency of results and applied forces as compared to most aluminum alloys commonly used in FSW such as Al-6061.

4.2 Weld Characteristics

Although narrowing down appropriate welding parameters proved to be difficult, the tensile tests showed that even the moderately successful weld obtained on this aluminum cerium alloy (Weld 3, **Figure 41**) had comparable ultimate tensile strength to the base material (up to 3.2 kN as compared to an average of 3.21 kN for the base plate). The tensile bar samples of the welded zone were additionally milled down to a small enough thickness (1/4-inch from 1/2-inch) to fit in the grips of the tensile tester, and it is suspected that any unmixed zones beneath the weld nugget that may have caused premature failure unrelated to the welded area (like the separation line seen in **Figure 46**) were eliminated during milling. Overall, the optical microscopy of the friction stir weld cross section showed anticipated dispersion of intermetallics and sufficient mixing of the two

plates, at least in the weld nugget and the TMAZ. Complete consolidation to the base of the joint would easily be attainable with either a larger tool or a thinner, more standard sized plate.

4.3 Viability for Commercial FSW Utilization

Although alloys such as the one studied in this thesis have higher mechanical property retention at high temperatures, it can be seen from the data provide here as well as from the literature survey of current research done on this alloy that the brittleness caused by the cerium intermetallics can be an issue when it comes overall strength and resistance to fatigue. Eck Industries was studying this particular alloy for potential use in piston development, but have since moved on to a comparable alloy composition with a lower cerium content; since the pistons would be under consistent high loading it was concluded that based on the data, the Al-10Si-7Ce-4.3Cu-0.4Mg alloy would be too brittle to withstand the operating conditions.

Work on aluminum cerium alloys is still continuing at Eck Industries; with lower cerium content, the material will regain some of its ductility, although at the expense of losing some of the mechanical property retention at high temperatures. For piston alloys, this appears to be the most logical move. There will be opportunities for applications of different compositions of these alloys depending on the components being analyzed and desired performance; for components that will undergo lower, more constant stresses in a high temperature environment, cerium content could likely be increased again until a certain safety limit is reached in which there is sufficient strength in addition to the high mechanical property retention. As much of the research on aluminum cerium alloys and how composition variations affect their behavior is still being conducted, it is anticipated that a variety of different versions of this alloy will be created with different optimal industrial applications depending on performance.

5 Conclusions

From the microstructural analysis, mechanical property testing, and friction stir welding results, it can be concluded that this aluminum cerium alloy can be successfully friction stir welded within a finely tuned process window. It can be reasonably assumed based on these results that with a highly controlled machine (capable of measuring and tracking applied torque and axial force), friction stir welding parameters could be calibrated for high quality butt welds of different variations of aluminum cerium alloys as well. All aluminum cerium alloys develop heavy, cerium-based intermetallic compounds with eutectic temperatures above 600ºC, which is suspected to be the reason that such high axial force and torque were required to fully plasticize and mix the alloy in the friction stir welding done in this thesis. Although it is more sensitive to variations of the process parameters as compared to other alloys commonly used in commercial FSW, successful welds can still be achieved. If aluminum cerium penetrates the aerospace industry and become utilized for creation high temperature environment components, FSW would be able to be utilized once a reliable process window was developed for the particular alloy in question.

REFERENCES

[1] Mishra, R. S. & Ma, Z. Y. Friction stir welding and processing. (2005). doi:10.1016/j.mser.2005.07.001

[2] Gibson, B. T. et al. Friction stir welding: Process, automation, and control. *J. Manuf. Process*. 16, 56–73 (2014).

[3] Sims, Z. C. *et al.* High-Performance Aluminum-Cerium Alloys for High-Temperature Applications. (2017).

[4] Sims, Z. C. et al. Cerium-Based, Intermetallic-Strengthened Aluminum Casting Alloy: High-Volume Co-product Development. *Journal of Manufacturing* 68, 1940–1947 (2016).

[5] Weiss, D., Rios, O., Sims, Z., Mccall, S. & Ott, R. Casting Characteristics of High Cerium Content Aluminum Alloys. doi:10.1007/978-3-319-51541-0_28

[6] S. P. Marsh and M. E. Glicksman, *Acta Materialia,* 1996, 44, 3761-3771.

[7] Cao, Z., Kong, G., Che, C., Wang, Y. & Peng, H. Experimental investigation of eutectic point in Al-rich Al-La, Al-Ce, Al-Pr and Al-Nd systems. *J. Rare Earths* 35, 1022–1028 (2017).

[8] Stroh, J., Davis, T., Mcdougal, A. & Sediako, D. In Situ Study of Solidification Kinetics of Al-Cu and Al-Ce-Mg Alloys with Application of Neutron Diffraction. (2018).

[9] Elgallad, E. M., Ibrahim, M. F., Doty, H. W. & Samuel, F. H. Microstructural characterisation of Al–Si cast alloys containing rare earth additions. *Philos. Mag.* **98,** 1337–1359 (2018).

[10] Luo, A.A. Magnesium: Current and potential automotive applications. *Journal of Manufacturing* 54 (2): 42-48. (2002)

[11] W.M. Griffith, R.E. Sanders, G.J. Hildeman. Elevated Temperature Aluminum Alloys for Aerospace Applications. High-strength powder metallurgy aluminum alloys, proceedings of a symposium sponsored by the powder metallurgy committee of the metallurgical society.

[12] J.G. Kaufman and E.L. Rooy, Aluminum Alloy Castings: Properties, Processes, and Applications (Materials Park, OH: *ASM International*, 2004).

[13] B. T. Gibson, Custom Low-Cost Force Measurement Methods in Friction Stir Welding, Vanderbilt University: M.S. Thesis, 2011.

[14] P. Sinclair, Heated Friction Stir Welding: An Investigation Into How Preheating Aluminum 6061 Affects Process Forces, Vanderbilt University: M.S. Thesis, 2009.

[15] Mendez, P. F., Tello, K. E., & Lienert, T. J. (2010). Scaling of coupled heat transfer and plastic deformation around the pin in friction stir welding. *Acta Materialia*, 6012-6026

[16] Guerra, M., Schmidt, C., McClure, J., Murr, L., & Nunes, A. (2003). Flow patterns during friction stir welding. *Materials Characterization*, 95-101.

[17] Colegrove, P., & Shercliff, H. (2004). Development of Trivex friction stir welding tool: Part 1 - two-dimensional flow modelling and experimental validation. Science and Technology of Welding and Joining, 345-351.

[18] Sorensen C, Nielsen B. Exploring geometry effects of convex scrolled shoulder, step spiral probe FSW tools, Friction stir welding and processing V. Warren- dale, PA: *The Minerals Metals & Materials Society*; 2009.

[19] ASTM E8 / E8M-16a, Standard Test Methods for Tension Testing of Metallic Materials, ASTM International, West Conshohocken, PA, 2016. doi: 10.1520/E0008_E0008M-16A

[20] Pei, X. J., & Dong, P. S. (2014). Shear localisation modelling of friction stir weld formation process. Science and Technology of Welding and Joining, 416-426.

APPENDIX

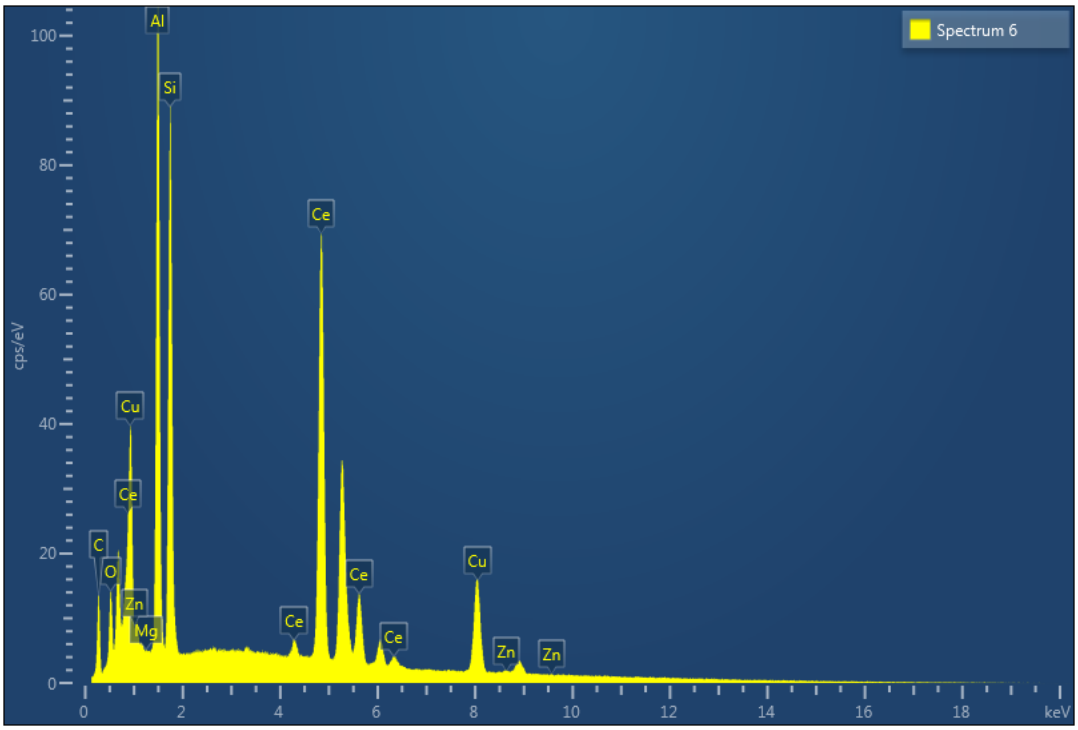

Figure 48. Point ID Spectrum 6

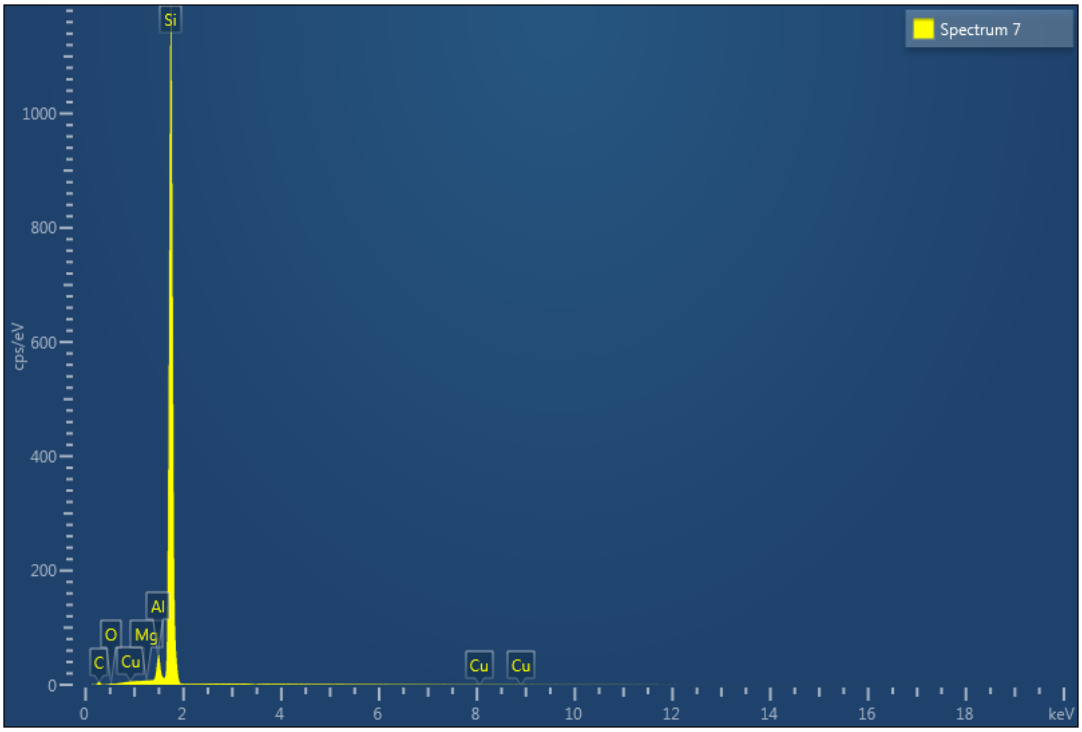

Figure 49. Point ID Spectrum 7

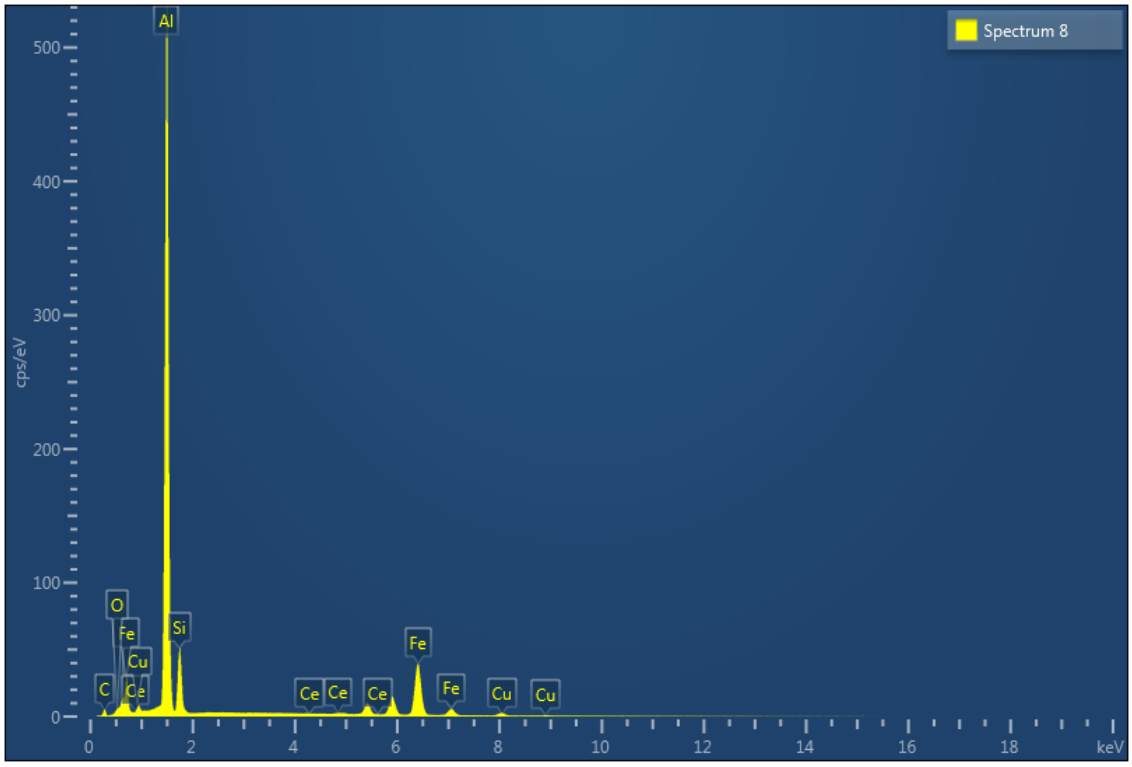

Figure 50. Point ID Spectrum 8

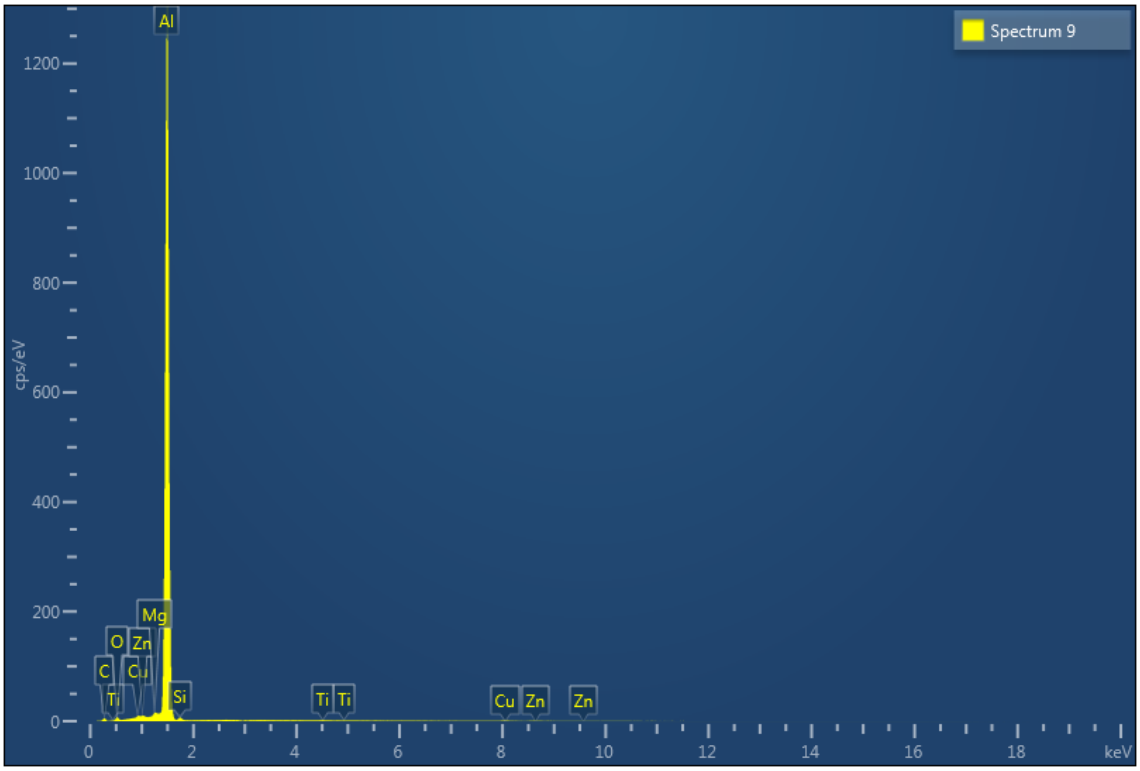

Figure 51. Point ID Spectrum 9

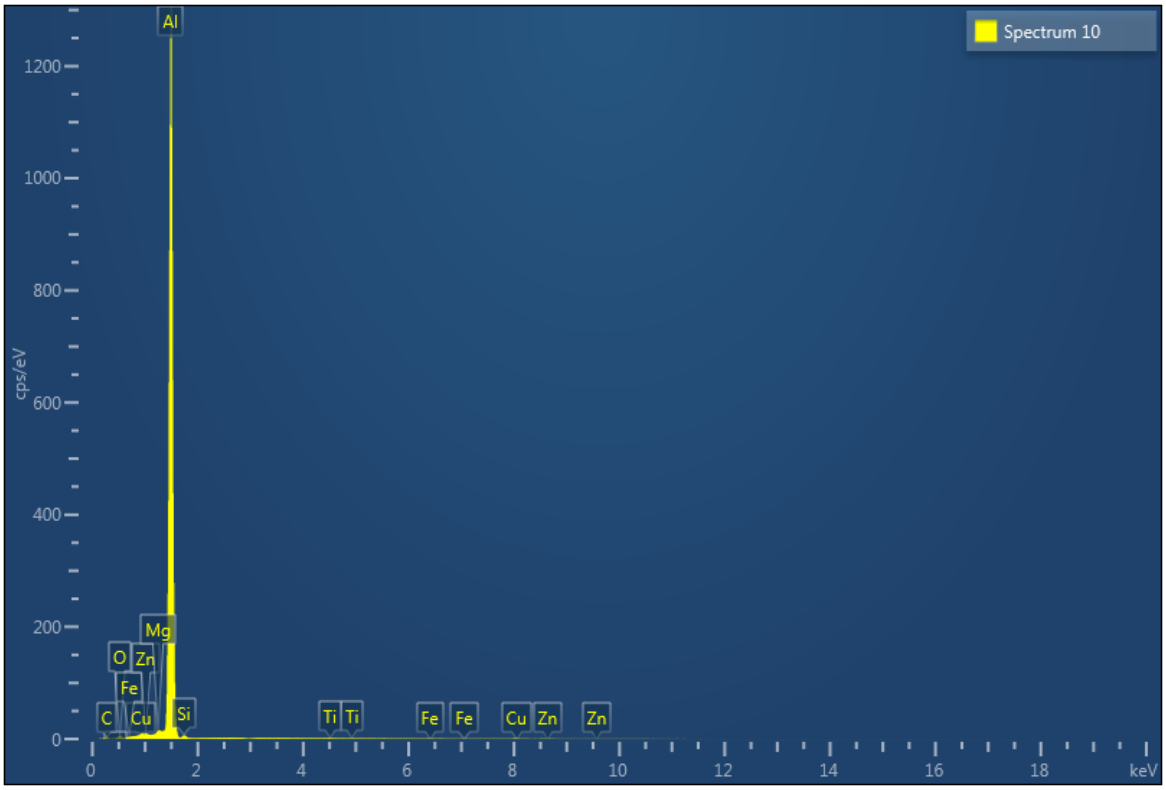

Figure 52. Point ID Spectrum 10

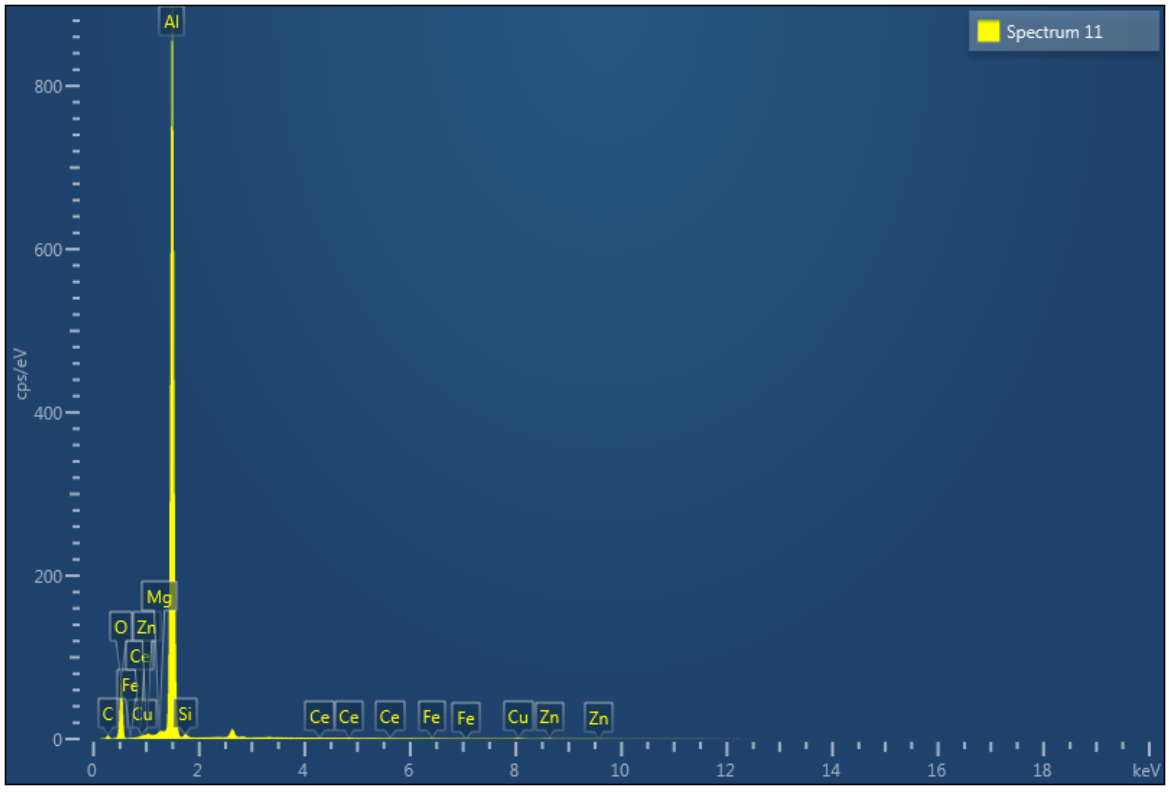

Figure 53. Point ID Spectrum 11

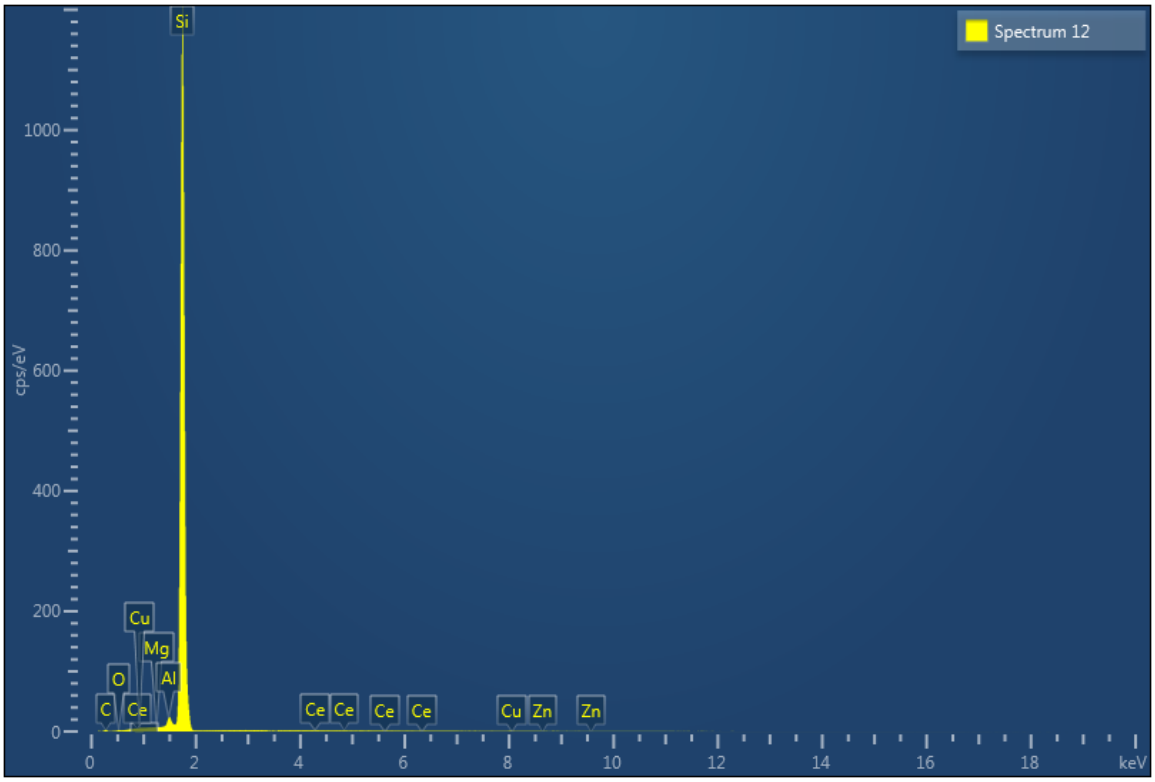

Figure 54. Point ID Spectrum 12

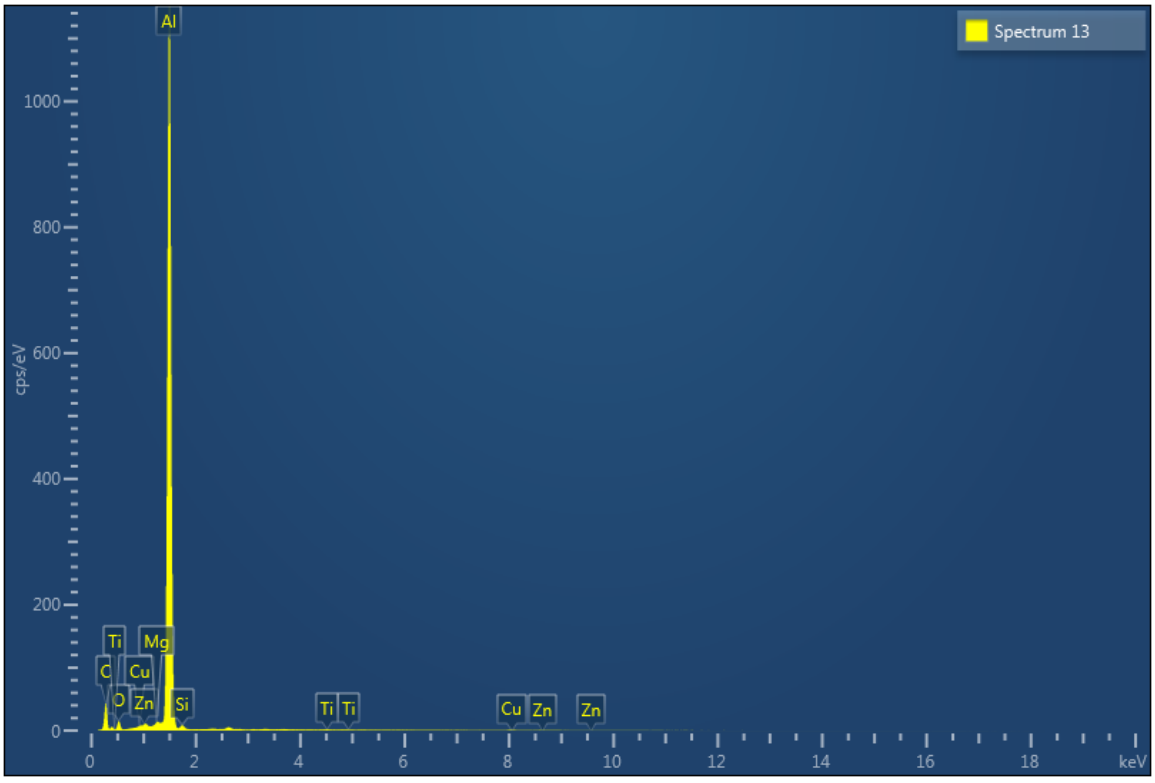

Figure 55. Point ID Spectrum 13

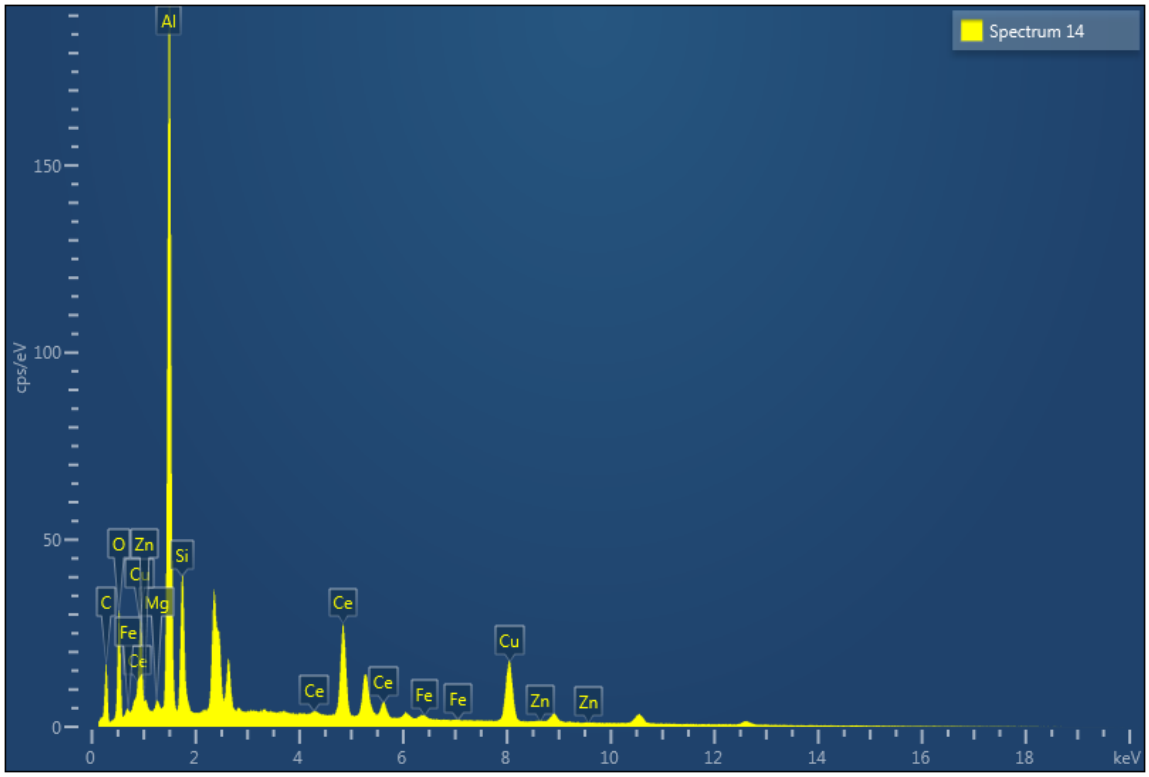

Figure 56. Point ID Spectrum 14

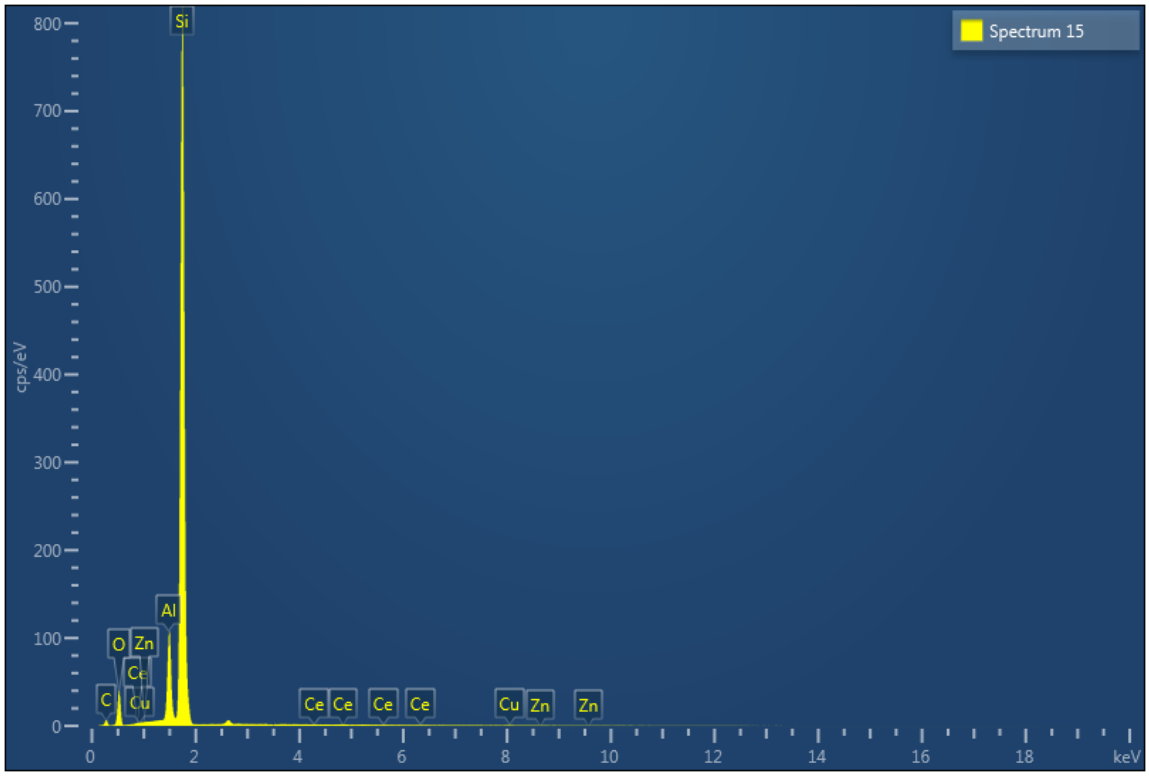

Figure 57. Point ID Spectrum 15

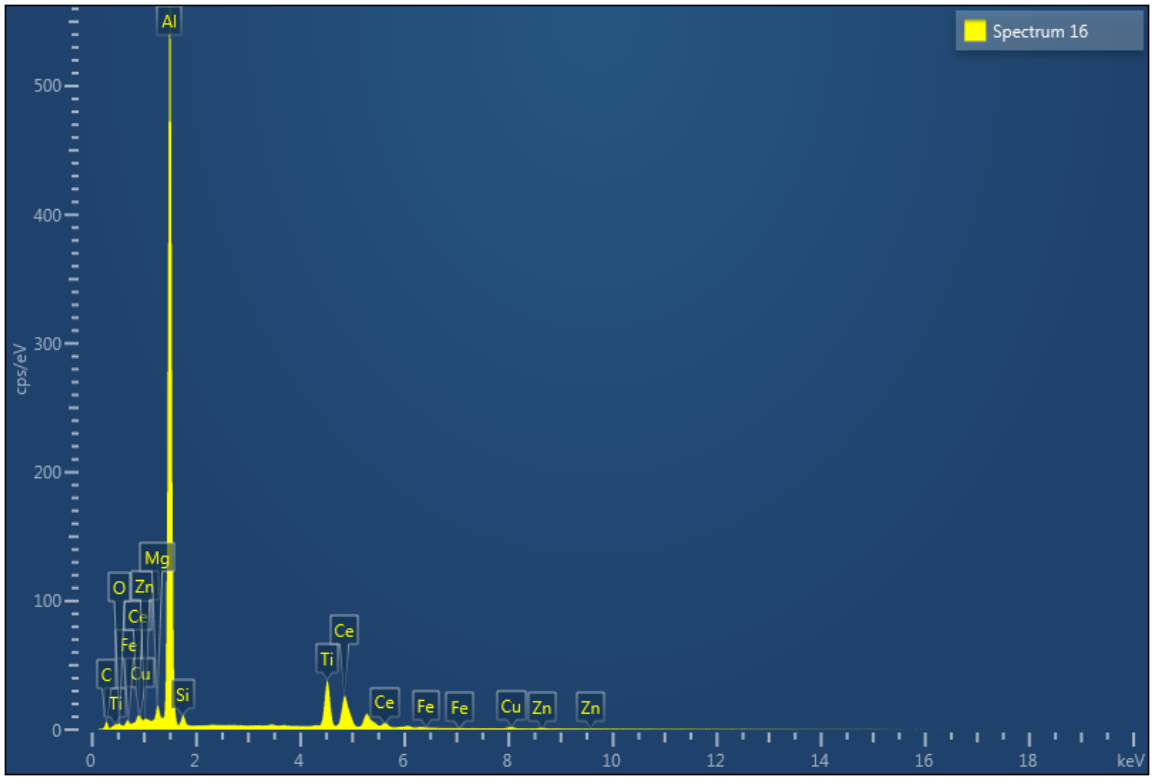

Figure 58. Point ID Spectrum 16

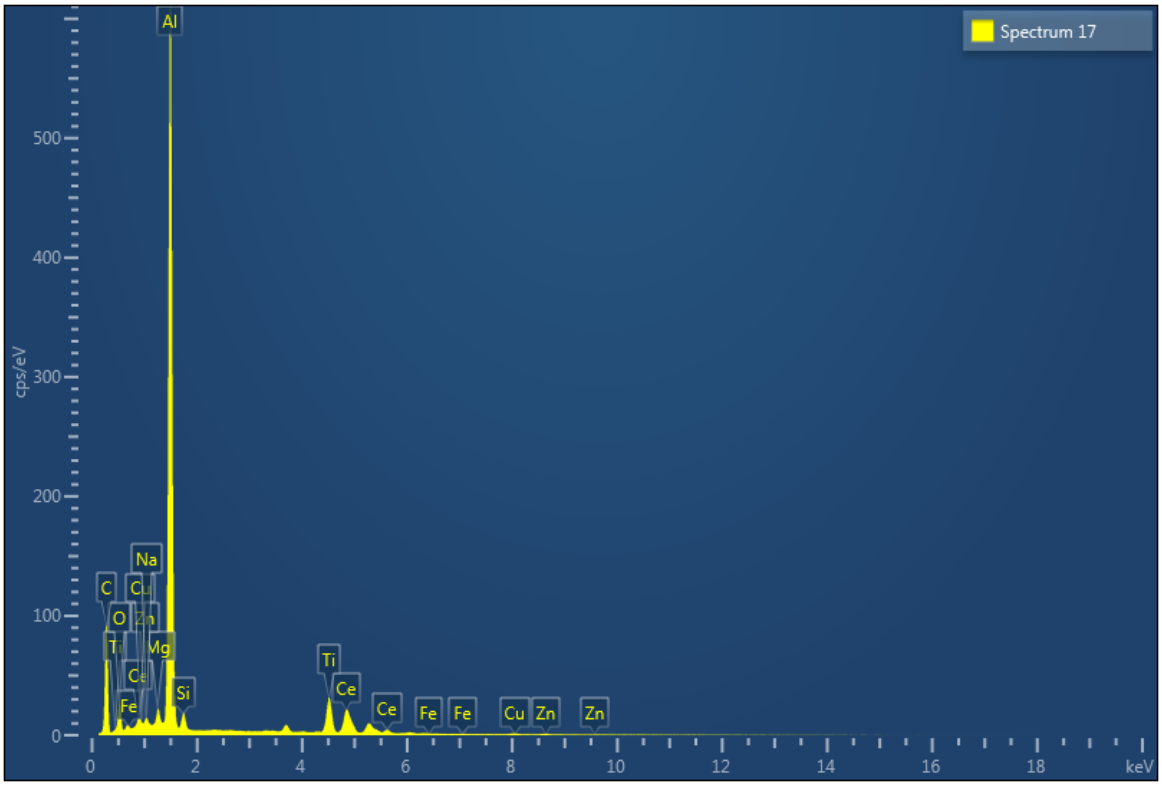

Figure 59. Point ID Spectrum 17

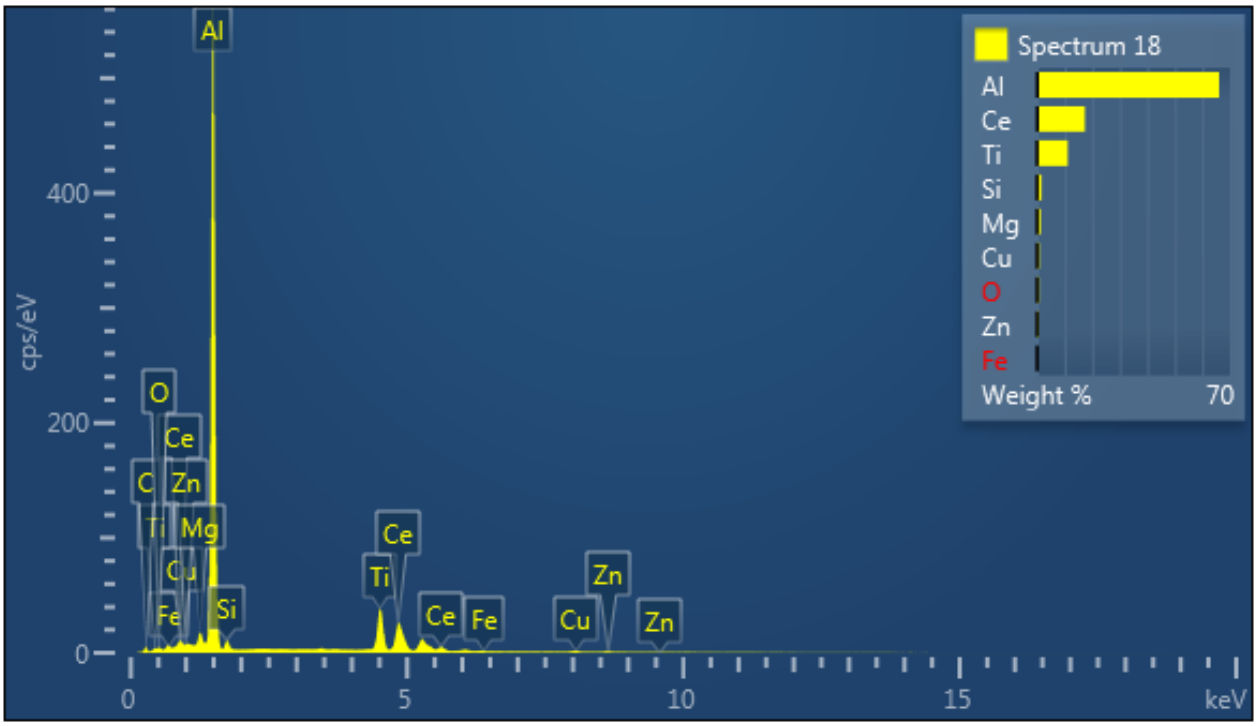

Figure 60. Point ID Spectrum 18

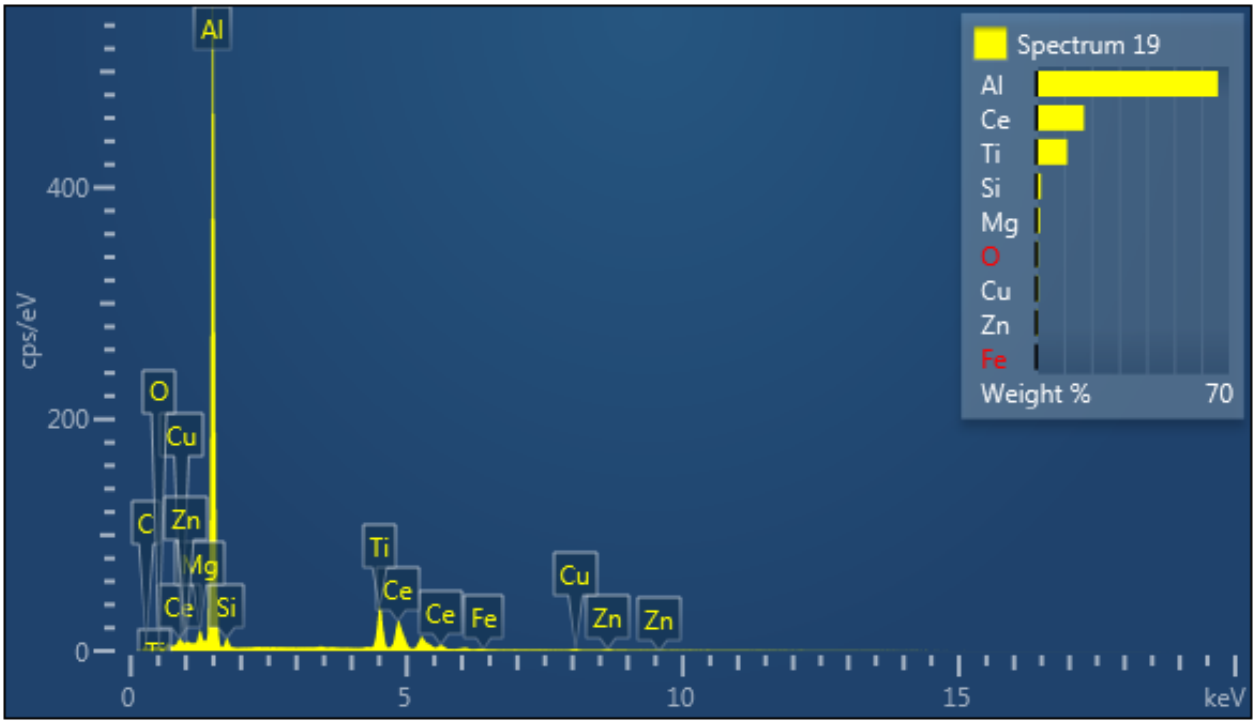

Figure 61. Point ID Spectrum 19

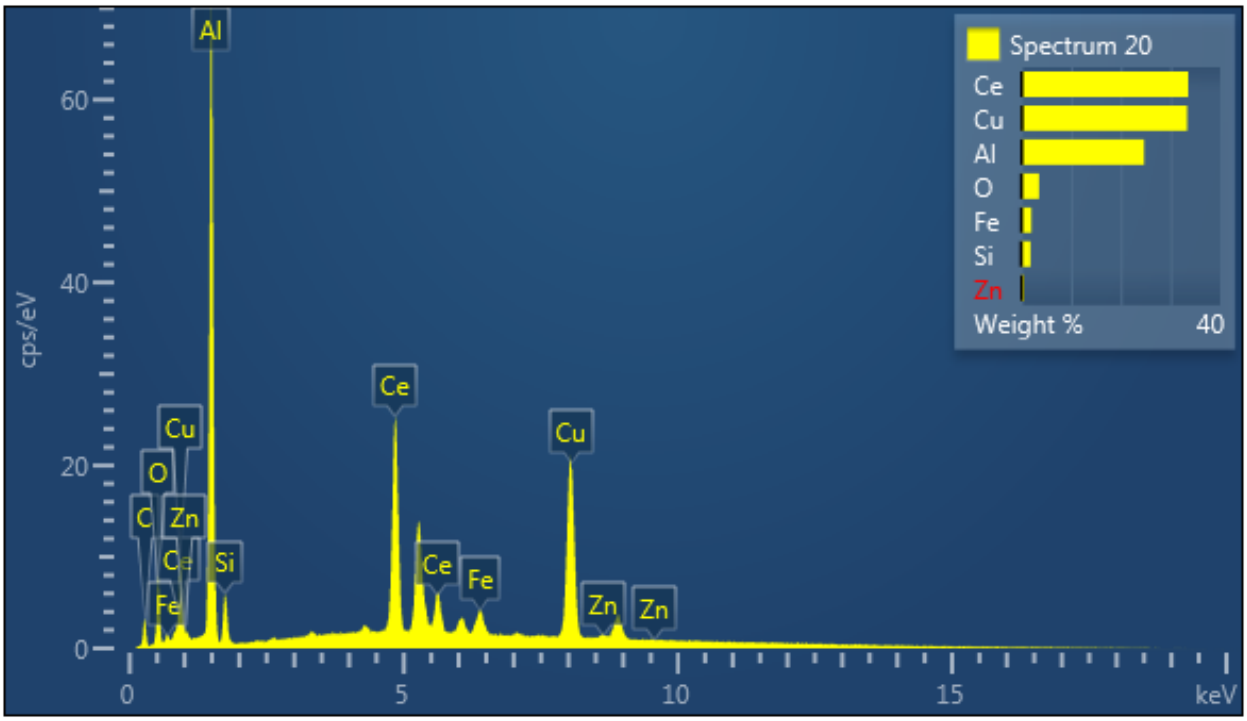

Figure 62. Point ID Spectrum 20

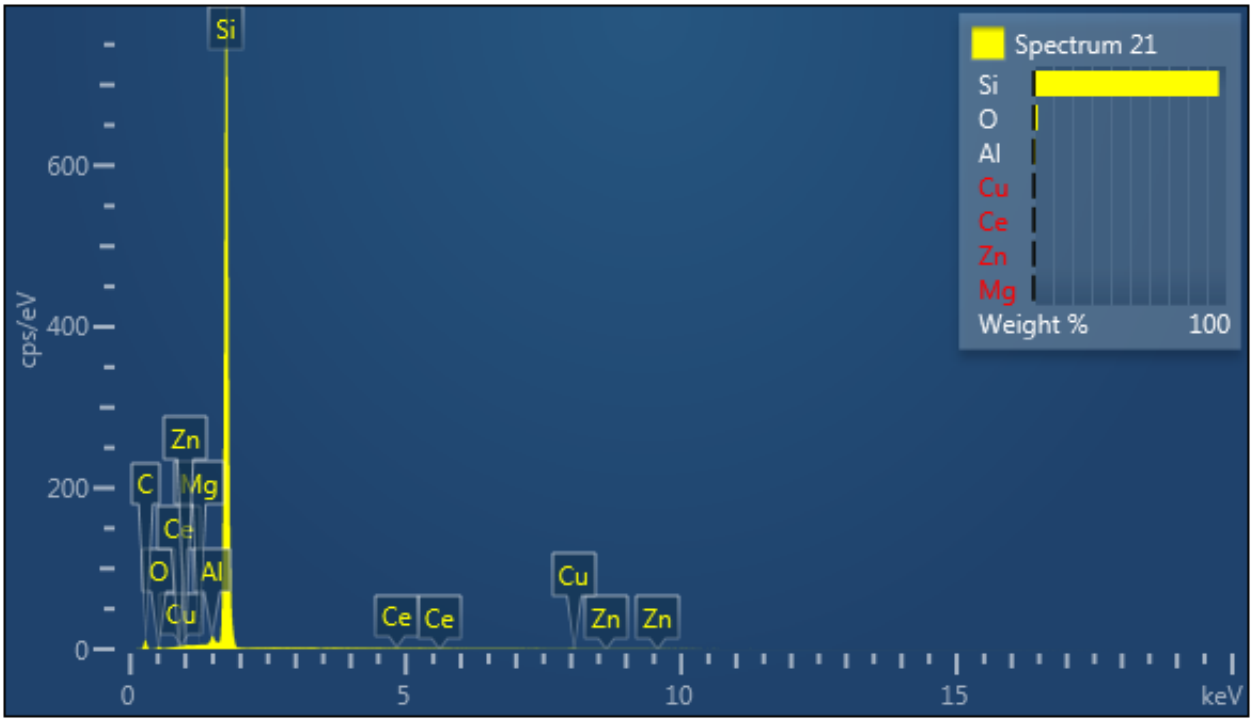

Figure 63. Point ID Spectrum 21

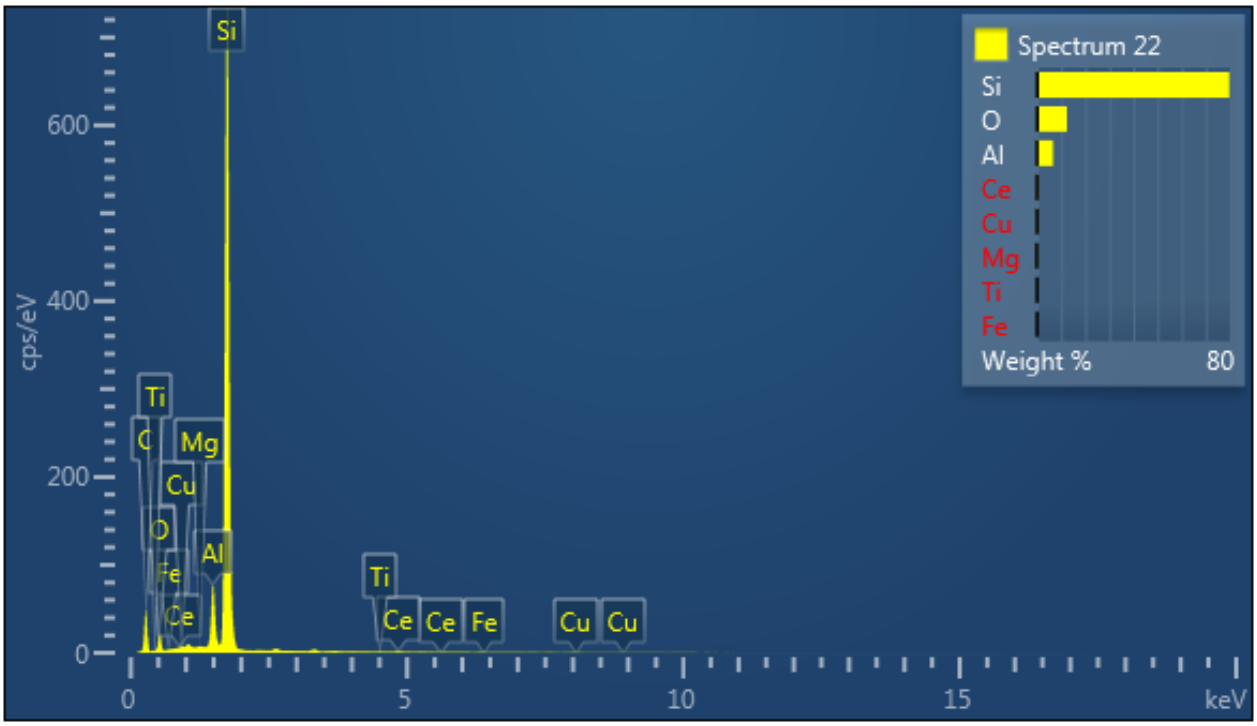

Figure 64. Point ID Spectrum 22

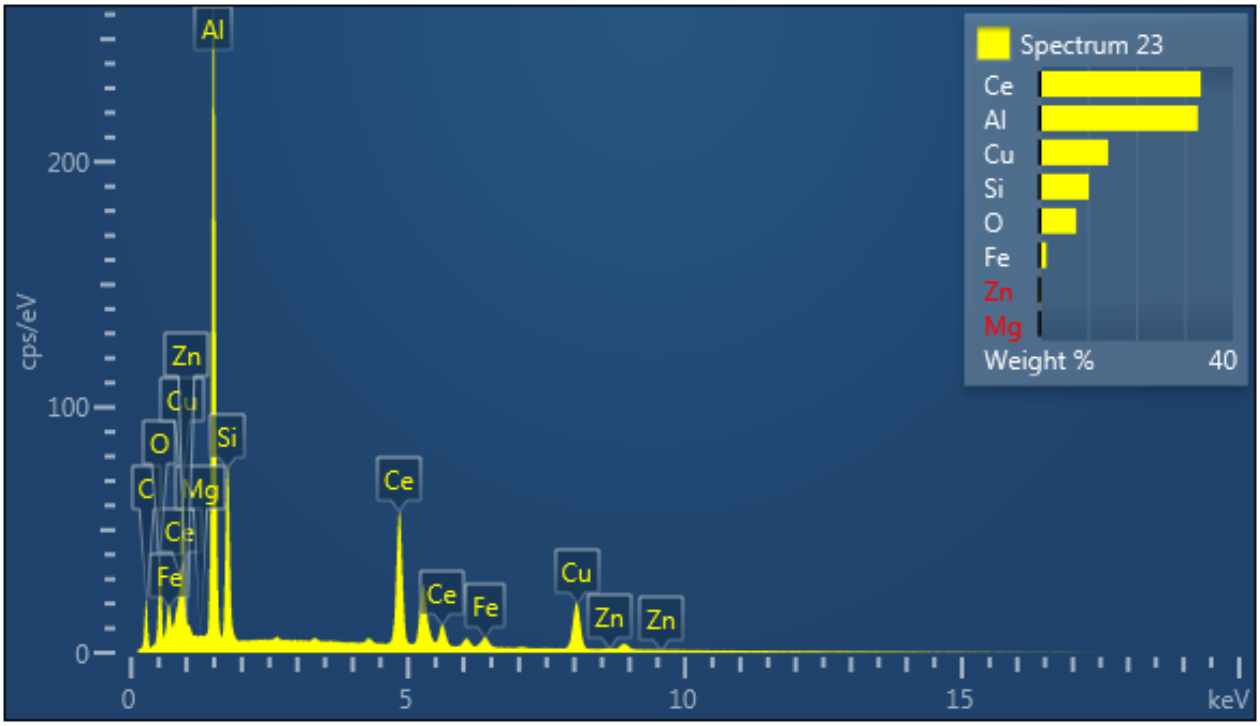

Figure 65. Point ID Spectrum 23